Interacting fermions on the honeycomb bilayer: From weak to strong coupling

Oskar Vafek
National High Magnetic Field Laboratory and Department of Physics, Florida State University, Tallahasse, Florida 32306, USA
(Received 12 August 2010; published 3 November 2010)

Many-body instabilities of the half-filled honeycomb bilayer are studied using weak-coupling renormalization group (RG) as well as strong-coupling expansion. For spinless fermions and assuming parabolic degeneracy, there are four independent four-fermion contact couplings. While the dominant instability depends on the microscopic values of the couplings, the broken symmetry state is typically a gapped insulator with either broken inversion symmetry or broken time-reversal symmetry, with a quantized anomalous Hall effect. Under certain conditions, the dominant instability may appear in the particle-particle (pairing) channel. For some nongeneric fine-tuned initial conditions, weak-coupling RG trajectories flow into the noninteracting fixed point, although generally we find runaway flows which we associate with ordering tendencies. Additionally, a tight-binding model with nearest-neighbor hopping and nearest-neighbor repulsion is studied in weak and strong couplings and in each regime a gapped phase with inversion symmetry breaking is found. In the strong-coupling limit, the ground-state wave function is constructed for vanishing in-plane hopping but finite inter-plane hopping, which explicitly displays the broken inversion symmetry and a finite difference between the number of particles on the two layers. Finally, we discuss the spin-1/2 case and use Fierz identities to show that the number of independent four-fermion contact couplings is 9. The corresponding RG equations in the spin-1/2 case are also presented, and used to show that, just as in strong coupling, the most dominant weak-coupling instability of the repulsive Hubbard model (at half filling) is an antiferromagnet.

DOI: 10.1103/PhysRevB.82.205106 PACS number(s): 71.10.−w, 71.45.−d

I. INTRODUCTION

The problem of interacting fermions on the *A*-*B* stacked honeycomb bilayer at half filling has attracted attention due to a confluence of several factors. First, purely on theoretical grounds, in its simplest form with the nearest-neighbor hoping only, the tight-binding approximation gives rise to a band structure with two bands touching *quadratically* at the Fermi level[1,2] near two nonequivalent points in the Brillouin zone, **K** and **K′**. Even at the noninteracting level, such quadratic degeneracy gives rise to logarithmically divergent susceptibilities[2,3] in several channels as temperature, or frequency, are taken to zero.[4–6] As a result, some form of spontaneous symmetry breaking is expected at finite temperature upon inclusion of even weak interactions.[2–8] And while fine tuning is necessary to achieve such band structure, in that (with the exception of square checkerboard and Kagome lattices studied in Ref. 8) inclusion of trigonal warping terms[1] eventually gives rise to four Dirac fermions at each **K** point, noninteracting susceptibilities may be sufficiently enhanced that many-body instabilities appear, albeit at finite coupling strength. In this sense, the *A*-*B* stacked honeycomb bilayer problem is another example of the observation that there are no *generic* weak-coupling particle-hole instabilities.[9] Rather, fine tuning, in the form of nesting, for example, is necessary to bring the strong-coupling physics down to weak coupling. If we are interested in accessing the symmetry-breaking phases in the particle-hole channel, as we *are* in this case, then fine tuning is a small price to pay for this access, made available within perturbative renormalization group (RG). Second, the isolation of graphene bilayers and the experimental ability to perform, for example, electrical,[10–12] angle resolved photoemission,[13] Raman spectroscopy,[14] or infrared[15] measurements, while controlling the gate voltage through the neutrality point, gives rise to the opportunity to test such theoretical expectations in a reasonably well controlled physical setting. In addition, the technological promise of this material fuels further need to understand its electronic structure and with it the many-body interactions. Finally, the problem of interacting fermions on the *AB*-stacked honeycomb bilayer may soon be realized in cold atom optical lattices, where the theory may also be tested.

The issue of band-structure fine-tuning notwithstanding, the type of leading instability in a graphene bilayer (with spin 1/2 fermions) has been a subject of debate as well. A mean-field approach has been used to argue for an insulating state with broken inversion symmetry.[7] A similar approach has also been argued to lead to trivial gapped insulating phases[5] as well as to an anomalous quantum Hall phase.[16] On the other hand, the leading weak-coupling instability can be analyzed without resorting to uncontrolled approximations by using weak-coupling renormalization group. This approach was used in Ref. 3 where a nematic phase was found to be the dominant instability within the model studied. Such instability was subsequently also argued for in Ref. 6. On the other hand, an inversion symmetry-breaking insulating phase has been claimed in Ref. 4.

To determine what type of broken symmetry state is preferred in the case of *spinless* fermions, we perform weak-coupling RG analysis by studying the flow of four-independent symmetry allowed short-range interactions. While some of the phases obtained here using a fully controlled weak-coupling RG analysis have been discussed before, either within mean-field or RG analysis, this work consistently analyzes the conditions under which few of these competing phases dominate over others. This is elaborated on in more detail below when discussing the flow diagram and the susceptibility analysis for the competing order parameters. We find that generically, depending on the initial

values of the four-fermion contact couplings, the system flows into a gapped phase with either broken inversion symmetry and a finite difference between the total number of particles on the two layers or broken time-reversal symmetry. The former state was not found to be preferred in the model for spin-1/2 fermions studied in Ref. 3 (where the nematic state was found to dominate) but an example of the latter state corresponded to one of the fixed points found therein. In particular, for the spinless case studied here, we find that a gapped state with anomalous (zero B-field) quantum Hall conductivity $\pm 2\frac{e^2}{h}$ has the most divergent susceptibility for a range of initial couplings as determined by the (right) sink of the RG trajectories shown in Fig. 3. While nongeneric, we also specify special conditions under which the interacting model flows back to the noninteracting fixed point.

In addition, we analyze the specific microscopic model with nearest-neighbor hopping(s) t (and $t_\perp$) and nearest-neighbor repulsion V in both the weak-coupling RG and in strong coupling. In both regimes we find the (trivial) insulating phase with broken inversion symmetry to dominate. As discussed in more detail below, in weak coupling the RG flow tends to the left sink shown in Fig. 3, with a susceptibility that dominates over other broken symmetry states mainly due to subdominant terms. In strong coupling, we construct a ground state wave function for $V>0$, $V_\perp>0$, $t=0$ but $t_\perp \neq 0$, which shows explicitly the broken layer inversion. Since in this model, the same symmetry appears to be broken in the limit of both weak and strong couplings, it is reasonable to assume that such a broken symmetry state appears at any V, $V_\perp>0$.

A similar analysis is presented in the spin-1/2 case with short-range interactions. For the repulsive Hubbard model, we find that the most dominant weak-coupling instability is toward an antiferromagnetic state. Since the same ordering tendency happens in the strong coupling, it is reasonable to assume that in this model, the Neel ordering appears at any $U>0$.

This paper is organized as follows: in Sec. II we write down the (noninteracting) bilayer Hamiltonian first in the tight-binding approximation and then within $\mathbf{k}\cdot\mathbf{p}$ perturbation theory. In Sec. III we construct the low-energy effective theory at the neutrality point by fine tuning the trigonal warping terms to zero. The rest of that section deals with identifying microscopic-symmetry-allowed four-fermion contact interaction terms using the method of Herbut *et al.*[17] used for the same purpose in single-layer graphene. Before the reduction due to Fierz identities, there are nine such couplings which further reduce to four once Fierz identities are taken into account. The weak-coupling RG is presented in Sec. IV, along with the flow diagram in the space of coupling constant ratios and the analysis of the susceptibility growth. The t-V model with weak- and strong-coupling limits is studied in Sec. V. In Sec. VI, the spin-1/2 case is revisited. Symmetry is used to construct an 18-dimensional Fierz vector along with the 18×18 Fierz matrix to show that there are nine independent couplings in this case. Their RG equations are determined and while more general, they are shown to reduce to the ones studied in Ref. 3 under conditions outlined therein. In Sec. VII we study the Hubbard model in weak and strong couplings. Section VIII is devoted to conclusions. Details of the derivation are presented in Appendices A and B.

II. BILAYER HAMILTONIAN

In this section we will define the noninteracting model by using two different approximation methods. First, the well-known tight-binding approximation[2] will be used and then the $\mathbf{k}\cdot\mathbf{p}$ method or equivalently the method of invariants.[1,6,18,19] Both methods lead to the same form of the low-energy Hamiltonian and it is ultimately a question of convenience which one should be adopted.

A. Tight-binding approximation

The noninteracting Hamiltonian in the tight-binding approximation can be written as

$$\mathcal{H}_0 = H_0^\perp + H_0^\parallel, \tag{1}$$

where

$$H_0^\perp = H_{0,0}^\perp + H_{0,1}^\perp + H_{0,2}^\perp, \tag{2}$$

$$H_{0,0}^\perp = t_\perp \sum_{\mathbf{R}} [a_1^\dagger(\mathbf{R}) a_2(\mathbf{R}) + \text{H.c.}], \tag{3}$$

$$H_{0,1}^\perp = t_\perp^{(1)} \sum_{\mathbf{R},\delta} [b_1^\dagger(\mathbf{R}+\delta) a_2(\mathbf{R}) + b_2^\dagger(\mathbf{R}-\delta) a_1(\mathbf{R}) + \text{H.c.}], \tag{4}$$

$$H_{0,2}^\perp = t_\perp^{(2)} \sum_{\mathbf{R},\delta} [b_1^\dagger(\mathbf{R}+\delta_1 z) b_2(\mathbf{R}+\delta_1+\delta) + \text{H.c.}], \tag{5}$$

$$H_0^\parallel = -t \sum_{\mathbf{R},\delta} [b_1^\dagger(\mathbf{R}+\delta) a_1(\mathbf{R}) + b_2^\dagger(\mathbf{R}-\delta) a_2(\mathbf{R}) + \text{H.c.}], \tag{6}$$

In the case of bilayer graphene, the values of the hopping integrals t, $t_\perp$, and $t_\perp^{(1,2)}$ were extracted experimentally in Ref. 20. If we define the Fourier transform of a Fermi field as $c_j(\mathbf{r}) = N_{uc}^{-1/2} \Sigma_{\mathbf{k}} e^{i\mathbf{k}\cdot\mathbf{r}} c_{j,\mathbf{k}}$, where $c=a$ or b, $j=1$ or 2, and N_{uc} is the number of unit cells. Next, we let $\chi_{\mathbf{k}}^\dagger = (a_{1,\mathbf{k}}^\dagger, a_{2,\mathbf{k}}^\dagger, b_{2,\mathbf{k}}^\dagger, b_{1,\mathbf{k}}^\dagger)$ to write the noninteracting Hamiltonian (1) as

$$\mathcal{H}_0 = \sum_{\mathbf{k}} \chi_{\mathbf{k}}^\dagger \begin{pmatrix} t_\perp & 0 & t_\perp^{(1)} d_{\mathbf{k}}^* & -t d_{\mathbf{k}} \\ 0 & t_\perp & -t d_{\mathbf{k}}^* & t_\perp^{(1)} d_{\mathbf{k}} \\ t_\perp^{(1)} d_{\mathbf{k}} & -t d_{\mathbf{k}} & 0 & t_\perp^{(2)} d_{\mathbf{k}}^* \\ -t d_{\mathbf{k}}^* & t_\perp^{(1)} d_{\mathbf{k}}^* & t_\perp^{(2)} d_{\mathbf{k}} & 0 \end{pmatrix} \chi_{\mathbf{k}}. \tag{7}$$

In the above, the wave-vector-dependent function $d_{\mathbf{k}} = \sum_\delta e^{i\mathbf{k}\cdot\delta}$ where the sum runs over $\delta_1 = \frac{\sqrt{3}}{2}\hat{x}a + \frac{1}{2}\hat{y}a$, $\delta_2 = -\frac{\sqrt{3}}{2}\hat{x}a + \frac{1}{2}\hat{y}a$, and $\delta_3 = -\hat{y}a$. Near $\mathbf{K}$, $d_{\mathbf{K}+\mathbf{k}} \approx -\frac{3}{2a} t(k_x + i k_y) = -v_F k_+$. Near $-\mathbf{K}$, $d_{-\mathbf{K}+\mathbf{k}} \approx \frac{3}{2a} t(k_x - i k_y) = v_F k_-$. The low-energy spectrum of this (well-known) Hamiltonian,[1,21] which is easily diagonalized, will be discussed in the next section.

B. k·p approach

Instead of resorting to the tight-binding approximation, we can also arrive at the low-energy Hamiltonian by analyz-

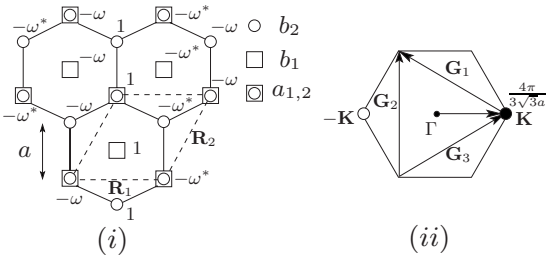

FIG. 1. (i) Schematic representation of the A-B stacked bilayer. The low-energy wave function near $\mathbf{K}$ is also sketched, with $\omega = e^{i\pi/3} = \frac{1}{2} + i\frac{\sqrt{3}}{2}$. The primitive lattice vectors are $\mathbf{R}_1 = \sqrt{3}a\hat{x}$ and $\mathbf{R}_2 = \frac{\sqrt{3}}{2}a\hat{x} + \frac{3}{2}a\hat{y}$. The area of the unit cell is $A_{uc} = \hat{z}\cdot(\mathbf{R}_1 \times \mathbf{R}_2) = \frac{3\sqrt{3}}{2}a^2$. (ii) Schematic representation of the (reciprocal) $\mathbf{k}$ space.

ing the symmetry of the bilayer potential alone. This is a standard technique when dealing with semiconductors[18] and one which has also been applied to graphene.[19] For the sake of self-inclusiveness, we present this method as well to show that one arrives at the same general form of the Hamiltonian as in the tight-binding approximation, although in practice the coefficients of various symmetry-allowed terms must be determined from experiment. We start with the Schrodinger equation for a particle moving in potential due to the atoms in layers 1 and 2 separated by $2c$

$$\mathcal{H}_0 = \frac{\mathbf{p}^2}{2m_e} + \frac{p_z^2}{2m_e} + V_1(\mathbf{r}) + V_2(\mathbf{r}), \tag{8}$$

where

$$V_1(\mathbf{r}) = \sum_{\mathbf{R}} [V_0(\mathbf{r} - \mathbf{R} - c\hat{z}) + V_0(\mathbf{r} - \mathbf{R} - \delta_1 - c\hat{z})], \tag{9}$$

$$V_2(\mathbf{r}) = \sum_{\mathbf{R}} [V_0(\mathbf{r} - \mathbf{R} + c\hat{z}) + V_0(\mathbf{r} - \mathbf{R} + \delta_1 + c\hat{z})]. \tag{10}$$

The low-energy field theory is written in terms of the eight-component Fermi fields (two layers, 1 and 2, two valleys, $\mathbf{K}$ and $-\mathbf{K}$, and two sublattices a and b as sketched in Fig. 1),

$$\Psi(\mathbf{r}) = \sum_{j=1,2} [u_{\mathbf{K}}^{(a_j)}(\mathbf{r})\psi_{\mathbf{K}}^{(a_j)}(\mathbf{r}) + u_{\mathbf{K}}^{(b_j)}(\mathbf{r})\psi_{\mathbf{K}}^{(b_j)}(\mathbf{r}) + u_{-\mathbf{K}}^{(a_j)}(\mathbf{r})\psi_{-\mathbf{K}}^{(a_j)}(\mathbf{r}) + u_{-\mathbf{K}}^{(b_j)}(\mathbf{r})\psi_{-\mathbf{K}}^{(b_j)}(\mathbf{r})]. \tag{11}$$

The rapidly varying Bloch functions at $\mathbf{K}$ and at $\mathbf{K}' = -\mathbf{K}$ are related by complex conjugation, $u_{\mathbf{K}}(\mathbf{r}) = u_{-\mathbf{K}}^*(\mathbf{r})$, irrespective of the layer or sublattice index. Moreover, the Bloch functions $u_{\mathbf{K}}^{a_j}(\mathbf{r})$ and $u_{\mathbf{K}}^{b_j}(\mathbf{r})$ transform irreducibly under point-group operations of the lattice (see Fig. 1). For the sake of concreteness, within the nearly free electron approximation for electron wave functions $|\chi_{1,2}\rangle$ confined to layers 1 and 2, respectively, we have

$$|u_{\mathbf{K}}^{(a_1)}\rangle = \frac{|\chi_1\rangle}{\sqrt{3}}(|\mathbf{K}\rangle + |\mathbf{K} + \mathbf{G}_1\rangle + |\mathbf{K} - \mathbf{G}_3\rangle), \tag{12}$$

$$|u_{\mathbf{K}}^{(b_1)}\rangle = \frac{|\chi_1\rangle}{\sqrt{3}}(|\mathbf{K}\rangle - \omega^*|\mathbf{K} + \mathbf{G}_1\rangle - \omega|\mathbf{K} - \mathbf{G}_3\rangle), \tag{13}$$

$$|u_{\mathbf{K}}^{(a_2)}\rangle = \frac{|\chi_2\rangle}{\sqrt{3}}(|\mathbf{K}\rangle + |\mathbf{K} + \mathbf{G}_1\rangle + |\mathbf{K} - \mathbf{G}_3\rangle), \tag{14}$$

$$|u_{\mathbf{K}}^{(b_2)}\rangle = \frac{|\chi_2\rangle}{\sqrt{3}}(|\mathbf{K}\rangle - \omega|\mathbf{K} + \mathbf{G}_1\rangle - \omega^*|\mathbf{K} - \mathbf{G}_3\rangle), \tag{15}$$

where $\omega = e^{i\pi/3} = \frac{1}{2} + i\frac{\sqrt{3}}{2}$,

$$\langle u_{\mathbf{K}}^{(a_j)}|\mathcal{H}_0|u_{\mathbf{K}}^{(a_j)}\rangle = \langle u_{\mathbf{K}}^{(b_j)}|\mathcal{H}_0|u_{\mathbf{K}}^{(b_j)}\rangle = E_0,$$

$$\langle u_{\mathbf{K}}^{(a_2)}|\mathcal{H}_0|u_{\mathbf{K}}^{(a_1)}\rangle = E_0 + \langle u_{\mathbf{K}}^{(a_2)}|\hat{V}_2|u_{\mathbf{K}}^{(a_1)}\rangle \equiv E_0 + t_\perp,$$

$$\langle u_{\mathbf{K}}^{(b_i)}|\mathcal{H}_0|u_{\mathbf{K}}^{(a_j)}\rangle = E_0, \tag{16}$$

i.e., the interlayer hopping arises from the mixing of the sublattices a_1 and a_2. The matrix elements of the in-plane momentum operator $\mathbf{p}$ are also dictated by symmetry to be

$$\langle u_{\mathbf{K}}^{(a_j)}|\mathbf{p}|u_{\mathbf{K}}^{(a_j)}\rangle = \langle u_{\mathbf{K}}^{(b_j)}|\mathbf{p}|u_{\mathbf{K}}^{(b_j)}\rangle = \langle u_{\mathbf{K}}^{(a_1)}|\mathbf{p}|u_{\mathbf{K}}^{(a_2)}\rangle = 0,$$

$$\langle u_{\mathbf{K}}^{(a_2)}|\mathbf{p}|u_{\mathbf{K}}^{(b_2)}\rangle = \langle u_{\mathbf{K}}^{(b_1)}|\mathbf{p}|u_{\mathbf{K}}^{(a_1)}\rangle \sim \hat{x} - i\hat{y},$$

$$\langle u_{\mathbf{K}}^{(a_1)}|\mathbf{p}|u_{\mathbf{K}}^{(b_2)}\rangle = \langle u_{\mathbf{K}}^{(b_1)}|\mathbf{p}|u_{\mathbf{K}}^{(a_2)}\rangle \sim \hat{x} - i\hat{y},$$

$$\langle u_{\mathbf{K}}^{(b_2)}|\mathbf{p}|u_{\mathbf{K}}^{(b_1)}\rangle \sim \hat{x} - i\hat{y}. \tag{17}$$

Defining $\xi_{\mathbf{K}}^\dagger(\mathbf{r}) = [\psi_{\mathbf{K}}^{(a_1)^\dagger}(\mathbf{r}), \psi_{\mathbf{K}}^{(a_2)^\dagger}(\mathbf{r}), \psi_{\mathbf{K}}^{(b_2)^\dagger}(\mathbf{r}), \psi_{\mathbf{K}}^{(b_1)^\dagger}(\mathbf{r})]$, gives us the effective Hamiltonian near $\mathbf{K}$ to read

$$\int d^2\mathbf{r}\,\xi_{\mathbf{K}}^\dagger(\mathbf{r}) \begin{pmatrix} 0 & t_\perp & v_2 k_- & v_F k_+ \\ t_\perp & 0 & v_F k_- & v_2 k_+ \\ v_2 k_+ & v_F k_+ & 0 & v_1 k_- \\ v_F k_- & v_2 k_- & v_1 k_+ & 0 \end{pmatrix} \xi_{\mathbf{K}}(\mathbf{r}). \tag{18}$$

This is equivalent to what we found in the tight-binding approximation.

The spectra of the $\mathbf{k}\cdot\mathbf{p}$ and the tight-binding Hamiltonians are well known and have been discussed extensively in the literature (see, e.g., Refs. 1, 2, and 20). In the vicinity of each $\mathbf{K}$ point, there are four Dirac points: one isotropic at $\pm\mathbf{K}$ and three anisotropic ones arranged in accordance with threefold lattice symmetry around the isotropic one. When we neglect trigonal warping terms, by setting $v_1 = v_2 = 0$, or set the higher order hopping terms $t_\perp^{(1)} = t_\perp^{(2)} = 0$, the four Dirac points merge into a parabolic degeneracy.

III. LOW-ENERGY EFFECTIVE THEORY

In the weak-coupling limit, the kinetic energy dictates which modes are important to determine the behavior of the system at low energies. Clearly, at $\mathbf{k} = 0$ we have two degenerate levels and two levels at $\pm t_\perp$. Since we wish to work with a theory for the low-energy modes only, we need to project out the bands which originate from the two "split-off" bands. We can do so in several equivalent ways. The method used here implements the path integral formalism, where we integrate out the Fermi fields associated with a_1 and a_2 modes (sites), and arrive at an effective action with an

effective "Hamiltonian" for the low-energy modes. In addition to the wave-vector dependence, this Hamiltonian is frequency dependent as well. Near the **K** point, the effective quadratic action after integrating out the a modes is

$$e^{-S^{(0)}_{eff}} = e^{-\int_0^\beta d\tau \psi^{b*}[\partial_\tau + H_{bb}]\psi^b} \times \int \mathcal{D}(\psi^{a*}\psi^a) e^{-\int_0^\beta d\tau (\psi^{a*}[\partial_\tau + H_{aa}]\psi^a + \psi^{a*}H_{ab}\psi^b + \psi^{b*}H_{ba}\psi^a)}.$$

Since the integral is Gaussian, we can easily perform it and find that up to an additive constant

$$S^{(0)}_{eff} = \frac{1}{\beta}\sum_n \psi^{b*}(i\omega_n)[-i\omega_n + H_{bb} - H_{ab}G_{aa}(i\omega_n)H_{ba}]\psi^b(i\omega_n),$$

where

$$H_{ab}G_{aa}(i\omega_n)H_{ba} = \frac{1}{t_\perp^2 + \omega_n^2}\begin{bmatrix} \mathcal{A}\mathbf{k}^2 & \mathcal{B}k_+^2 \\ \mathcal{B}k_-^2 & \mathcal{A}\mathbf{k}^2 \end{bmatrix}, \tag{19}$$

$$\mathcal{A} = [i\omega_n(v_F^2 + v_2^2) + 2t_\perp v_F v_2], \tag{20}$$

$$\mathcal{B} = [t_\perp(v_F^2 + v_2^2) + 2i\omega_n v_F v_2], \tag{21}$$

and

$$H_{bb} = \begin{bmatrix} 0 & v_1 k_- \\ v_1 k_+ & 0 \end{bmatrix}. \tag{22}$$

Within the $\mathbf{k}\cdot\mathbf{p}$ theory, the parameters v_1 and v_2 should be determined from experiment. To make contact with the notation in literature, Ref. 21 have $v_1=v_3$ and $v_2=-v_4$ [see their Eqs. (6) and (15)].

If we are interested in the modes near the Fermi level of an unbiased bilayer, we can simply set $\omega_n=0$ in the effective action [Eqs. (19)–(22)]. As will be obvious from the discussion in the next section, terms arising from the corrections are perturbatively irrelevant near the Gaussian fixed point in the sense discussed in a different context in Ref. 22.

In what follows we will also set $v_1=v_2=0$ to fine tune the system to quadratic degeneracy. Such a situation arises if in the tight-binding formulation we consider only the nearest-neighbor hopping integrals, t and $t_\perp$. Otherwise, as mentioned in Sec. I, the ultimate low-energy dispersion involves four (one isotropic and three anisotropic) Dirac cones.[1,6,21] While such fine tuning appears artificial, it is an example of the maxim[9] that there are no *generic* weak-coupling particle-hole instabilities. Rather, fine tuning, in the form of nesting, for example, is necessary to bring the strong-coupling physics down to weak coupling. If we are interested in accessing the symmetry-breaking phases in the particle-hole channel, as we *are* in this case, then fine tuning is a small price to pay for this access made available within perturbative RG.[9]

Putting back the $-\mathbf{K}$ point, the low-energy degrees of freedom can now be expressed in terms of a four component Fermi field

$$\psi^\dagger(\mathbf{r}) = [\psi^{(b_1)^\dagger}_{\mathbf{K}}(\mathbf{r}), \psi^{(b_2)^\dagger}_{\mathbf{K}}(\mathbf{r}), \psi^{(b_1)^\dagger}_{-\mathbf{K}}(\mathbf{r}), \psi^{(b_2)^\dagger}_{-\mathbf{K}}(\mathbf{r})],$$

i.e., the electronic degrees of freedom are expanded as

$$\tilde{\Psi}(\mathbf{r}) = \sum_{j=1,2}[u^{(b_j)}_{\mathbf{K}}(\mathbf{r})\psi^{(b_j)}_{\mathbf{K}}(\mathbf{r}) + u^{(b_j)}_{-\mathbf{K}}(\mathbf{r})\psi^{(b_j)}_{-\mathbf{K}}(\mathbf{r})]. \tag{23}$$

The noninteracting low-energy (imaginary time τ) Lagrangian, which includes both K and K′ valleys, and which will serve as our (Gaussian) fixed point of departure, can therefore be written as

$$\mathcal{L}_0 = \int d^2\mathbf{r}\left[\psi^\dagger(\tau,\mathbf{r})\left(\frac{\partial}{\partial\tau} + \sum_{a=x,y}\Sigma^a d^a_{\mathbf{p}}\right)\psi(\tau,\mathbf{r})\right], \tag{24}$$

where we defined the vector function $\mathbf{d_k}$ and the 4×4 matrices $\Sigma^{x,y}$ as

$$d^x_{\mathbf{k}} = \frac{k_x^2 - k_y^2}{2m}, \quad d^y_{\mathbf{k}} = -\frac{2k_x k_y}{2m}, \tag{25}$$

$$\Sigma^x = 1\sigma^x = \gamma_2, \quad \Sigma^y = \tau^z\sigma^y = \gamma_1. \tag{26}$$

The effective-mass parameter entering the above equations is $m=t_\perp/(2v_F^2)$ [in the tight-binding approximation $v_F=3t/(2a)$]. The four component Fermi objects ψ appearing in Eq. (24) were defined as the envelope Fermi fields in Eq. (23). In the above, the first Pauli matrix acts in the valley $\pm\mathbf{K}$ space and the second in the layer 1,2 space. To make contact with the literature we also use Dirac γ matrices which we represent as

$$\gamma_0 = 1\sigma^z, \tag{27}$$

$$\gamma_1 = \tau^z\sigma^y, \tag{28}$$

$$\gamma_2 = 1\sigma^x, \tag{29}$$

$$\gamma_3 = \tau^x\sigma^y, \tag{30}$$

$$\gamma_5 = \tau^y\sigma^y. \tag{31}$$

The action $\int d\tau\mathcal{L}_0$ is invariant under the scale transformation

$$\mathbf{r} \to s\mathbf{r}, \tag{32}$$

$$\tau \to s^2\tau, \tag{33}$$

$$\psi \to s^{-1}\psi. \tag{34}$$

This means that the "dynamical critical exponent" $z=2$ for the Gaussian theory, which will be our point of departure when analyzing *weak-coupling* instabilities.

Short-range interactions

From the above discussion of the Gaussian fixed point, it is evident that the short-range interactions, when projected onto our low-energy modes, will contain among other (perturbatively irrelevant) terms, contact four-fermion terms which are marginal by power counting. The rest of this section deals with identifying such symmetry-allowed interaction terms. The method used here follows almost verbatim the method used by Herbut *et al.*[17] in their analysis of the

short-range interactions in *single-layer* graphene. In addition to the lattice symmetries used in Ref. 17, we also include the threefold rotational symmetry,[19] which reduces the number of independent four-fermion couplings to 4.

We can therefore start by writing the general Lagrangian

$$\mathcal{L} = \mathcal{L}_0 + \mathcal{L}_{int}, \tag{35}$$

where $\mathcal{L}_0$ was introduced in Eq. (24) and

$$\mathcal{L}_{int} = \frac{1}{2}\sum_{S,T} g_{ST} \int d^2\mathbf{r}[\psi^\dagger S\psi(\mathbf{r},\tau)][\psi^\dagger T\psi(\mathbf{r},\tau)], \tag{36}$$

where, at this point, the sum over S includes all 16 independent four-by-four matrices [generators of $SU(4)$] and so does the sum over T. Naively, we have $16+8\times 15=136$ couplings to consider. Just as in the case of the single-layer graphene,[17] this number will be dramatically reduced first by using the discrete symmetries of the lattice and second by using Fierz identities.

The key role in this reduction is played by the behavior of the Bloch functions $u(\mathbf{r})$ under symmetry operations, which dictates the transformation properties of the four component, slowly varying, envelope Fermi fields $\psi(\mathbf{r})$.[18,19] The dimer centered rotation by $2\pi/3$, mirror reflection about the yz plane and about the xz axis followed by xy plane, respectively, give

$$\hat{C}_3\psi(x,y) = -e^{-i(\pi/3)\tau_3\sigma_3}\psi\left(-\frac{1}{2}x-\frac{\sqrt{3}}{2}y,\frac{\sqrt{3}}{2}x-\frac{1}{2}y\right)$$

$$= -e^{(\pi/3)\gamma_1\gamma_2}\psi\left(-\frac{1}{2}x-\frac{\sqrt{3}}{2}y,\frac{\sqrt{3}}{2}x-\frac{1}{2}y\right), \tag{37}$$

$$\hat{\sigma}_v^y\psi(x,y) = \tau_1 1_2\psi(-x,y) = i\gamma_1\gamma_5\psi(-x,y), \tag{38}$$

$$\hat{\sigma}_v^z\hat{\sigma}_v^x\psi(x,y) = 1_2\sigma_1\psi(x,-y) = \gamma_2\psi(x,-y), \tag{39}$$

The time-reversal symmetry and translational symmetry give

$$\Theta\psi(\mathbf{r}) = \tau_1 1_2\psi^*(\mathbf{r}) = i\gamma_1\gamma_5\psi^*(\mathbf{r}), \tag{40}$$

$$\hat{t}\psi(\mathbf{r}) = e^{i\mathbf{K}\cdot\mathbf{R}\tau_3 1_2}\psi(\mathbf{r}+\mathbf{R}) = e^{\mathbf{K}\cdot\mathbf{R}\gamma_3\gamma_5}\psi(\mathbf{r}+\mathbf{R}). \tag{41}$$

In the above, $\mathbf{R}=m\mathbf{R}_1+n\mathbf{R}_2$ where $\mathbf{R}_1=\sqrt{3}a\hat{x}$ and $\mathbf{R}_2=\frac{\sqrt{3}}{2}a\hat{x}+\frac{3}{2}a\hat{y}$. And since $\mathbf{K}=\frac{4\pi}{3\sqrt{3}a}\hat{x}$, $\mathbf{K}\cdot\mathbf{R}=\frac{2\pi}{3}(2m+n)$, where $m,n=0,\pm 1,\pm 2,\ldots$. The lattice translational symmetry therefore corresponds to the Z_3 discrete analog of the chiral $U_c(1)$ generated by $\gamma_3\gamma_5$.

1. Symmetry reduction

Following Herbut *et al.*,[17] we split the 16 linearly independent four-by-four matrices S and T into four sets

$$A = \{1_4, \gamma_2, i\gamma_0\gamma_3, i\gamma_1\gamma_5\}, \tag{42}$$

$$B = \{i\gamma_0\gamma_1, -i\gamma_3\gamma_5, i\gamma_0\gamma_5, i\gamma_1\gamma_3\}, \tag{43}$$

$$C = \{\gamma_0, i\gamma_0\gamma_2, \gamma_3, i\gamma_2\gamma_3\}, \tag{44}$$

$$D = \{\gamma_1, i\gamma_1\gamma_2, \gamma_5, i\gamma_2\gamma_5\}. \tag{45}$$

The matrices which belong to the set A are even under both reflection operations [Eqs. (38) and (39)]. The matrices in the set B are odd under y reflections [Eq. (38)] and even under "x" reflections [Eq. (39)]. The matrices in the set C are even under y reflections [Eq. (38)] and odd under x reflections [Eq. (39)]. And finally, matrices belonging to the set D are odd under both Eqs. (38) and (39). This means that only quartic terms combining matrices from the same set are allowed by symmetry. Each such set contains $4+2\times 3=10$ such terms and that leaves 40 couplings.

Eight matrices $A_{1,2}$, $B_{1,2}$, $C_{1,2}$, and $D_{1,2}$ are left invariant under the spatial translation operation (41). These give rise to $3\times 4=12$ couplings, eight direct $g_{X_jX_j}$ ($X=A$, B, C, or D and $j=1$ or 2), as well as four mixed $g_{X_1X_2}$. In addition, there are four sets of pairs which transform as vectors under Eq. (41), $\alpha=\{A_3,B_3\}$, $\beta=\{B_4,A_4\}$, $\gamma=\{C_3,D_3\}$, and $\delta=\{C_4,D_4\}$. These give rise to additional six couplings. Schematically, four of them are $\Sigma_{\rho=\alpha,\beta,\gamma,\delta}\Sigma_{j=1}^2 g_\rho\rho_j\otimes\rho_j$ and two mixed ones are $g_{\alpha\beta}(A_3\otimes A_4-B_3\otimes B_4)$ and $g_{\gamma\delta}(C_3\otimes C_4+D_3\otimes D_4)$. Altogether, after inclusion of the translation symmetry, we are left with 18 couplings.

The unitary part of the time-reversal operations Θ, Eq. (40), happens to correspond to the mirror reflection about y, [Eq. (38)], which has already been taken into account. However, complex conjugation, further restricts the number of couplings. Specifically, mixed terms with one purely real and one purely imaginary matrix cannot appear, therefore $g_{C_1C_2}=g_{D_1D_2}=g_{\gamma\delta}=0$. This leaves 15 couplings.[17]

The lattice symmetries considered by Herbut *et al.*[17] did not contain site- or plaquette-centered rotation[19] by 120°. As stated in Eq. (37), this symmetry is generated by $i\gamma_1\gamma_2$. Including this symmetry requires that the cross terms $g_{A_1A_2}=g_{B_1B_2}=g_{\alpha\beta}=0$. Moreover, it requires that $g_{A_2A_2}=g_{D_1D_1}$, $g_{B_1B_1}=g_{C_2C_2}$, and $g_\beta=g_\delta$.

This leaves us with the following nine terms:

$$\begin{aligned}
&g_{A_1A_1}(\psi^\dagger A_1\psi)^2 + g_{A_2A_2}[(\psi^\dagger A_2\psi)^2 + (\psi^\dagger D_1\psi)^2] \\
&+ g_{B_1B_1}[(\psi^\dagger B_1\psi)^2 + (\psi^\dagger C_2\psi)^2] + g_{B_2B_2}(\psi^\dagger B_2\psi)^2 \\
&+ g_{C_1C_1}(\psi^\dagger C_1\psi)^2 + g_{D_2D_2}(\psi^\dagger D_2\psi)^2 + g_\alpha[(\psi^\dagger A_3\psi)^2 \\
&+ (\psi^\dagger B_3\psi)^2] + g_\gamma[(\psi^\dagger C_3\psi)^2 + (\psi^\dagger D_3\psi)^2] + g_\beta[(\psi^\dagger B_4\psi)^2 \\
&+ (\psi^\dagger A_4\psi)^2 + (\psi^\dagger C_4\psi)^2 + (\psi^\dagger D_4\psi)^2].
\end{aligned} \tag{46}$$

The nine terms can be further reduced to four independent ones by using Fierz identities.

2. Fierz identities

We set $g_{XX}=g_X$ to continue with the notation of Ref. 17. We use the method employed therein to write down Fierz identities[17,23] which, due to the Grassman nature of the Fermi fields, relate various seemingly unrelated couplings.

The starting point is the $SU(4)$ algebraic identity [see Eq. (A4) of Ref. 17]

$$S_{ij}T_{mn} = \frac{1}{16}\mathrm{Tr}[S\Gamma^a T\Gamma^b]\Gamma^b_{in}\Gamma^a_{mj}, \tag{47}$$

which leads to

$$[\psi^\dagger(x)S\psi(x)][\psi^\dagger(y)T\psi(y)] = -\frac{1}{16}\mathrm{Tr}[S\Gamma^a T\Gamma^b][\psi^\dagger(x)\Gamma^b\psi(y)] \times[\psi^\dagger(y)\Gamma^a\psi(x)]. \tag{48}$$

The minus sign comes from ψ and $\psi^\dagger$ being anticommuting (four component) Grassman fields. For contact terms $x=y$ and the above Eq. (48) constitutes a set of linear relations between different terms of our symmetry reduced interaction Lagrangian [Eq. (46)].

If we arrange the quartic terms into a vector

$$\begin{aligned} V = \{&(\psi^\dagger A_1\psi)^2, (\psi^\dagger A_2\psi)^2 + (\psi^\dagger D_1\psi)^2, (\psi^\dagger B_1\psi)^2 \\ &+ (\psi^\dagger C_2\psi)^2, (\psi^\dagger B_2\psi)^2, (\psi^\dagger C_1\psi)^2, (\psi^\dagger D_2\psi)^2, (\psi^\dagger A_3\psi)^2 \\ &+ (\psi^\dagger B_3\psi)^2, (\psi^\dagger B_4\psi)^2 + (\psi^\dagger A_4\psi)^2 + (\psi^\dagger C_4\psi)^2 \\ &+ (\psi^\dagger D_4\psi)^2, (\psi^\dagger C_3\psi)^2 + (\psi^\dagger D_3\psi)^2\}, \end{aligned} \tag{49}$$

then the Fierz identities lead to the linear constraint

$$FV = 0. \tag{50}$$

A straightforward, though somewhat laborious, application of Eq. (48) leads to the explicit form of the Fierz matrix in the case of spinless fermions

$$F = \begin{pmatrix} 5 & 1 & 1 & 1 & 1 & 1 & 1 & 1 & 1 \\ 2 & 4 & 0 & 2 & -2 & -2 & 2 & 0 & -2 \\ 2 & 0 & 4 & 2 & -2 & -2 & -2 & 0 & 2 \\ 1 & 1 & 1 & 5 & 1 & 1 & -1 & -1 & -1 \\ 1 & -1 & -1 & 1 & 5 & 1 & -1 & 1 & -1 \\ 1 & -1 & -1 & 1 & 1 & 5 & 1 & -1 & 1 \\ 2 & 2 & -2 & -2 & -2 & 2 & 4 & 0 & 0 \\ 4 & 0 & 0 & -4 & 4 & -4 & 0 & 4 & 0 \\ 2 & -2 & 2 & -2 & -2 & 2 & 0 & 0 & 4 \end{pmatrix}. \tag{51}$$

The matrix F has four zero eigenvalues and as a result there are four independent couplings.[17]

In order to make a connection with the previous work,[3] we choose to eliminate

$$\begin{aligned} (\psi^\dagger B_1\psi)^2 + (\psi^\dagger C_2\psi)^2 = &-2(\psi^\dagger A_1\psi)^2 + [(\psi^\dagger A_2\psi)^2 \\ &+ (\psi^\dagger D_1\psi)^2] - 2(\psi^\dagger D_2\psi)^2 \\ &- 2[(\psi^\dagger C_3\psi)^2 + (\psi^\dagger D_3\psi)^2], \end{aligned} \tag{52}$$

$$\begin{aligned} (\psi^\dagger B_2\psi)^2 = &-[(\psi^\dagger A_2\psi)^2 + (\psi^\dagger D_1\psi)^2] + (\psi^\dagger D_2\psi)^2 \\ &+ [(\psi^\dagger C_3\psi)^2 + (\psi^\dagger D_3\psi)^2], \end{aligned} \tag{53}$$

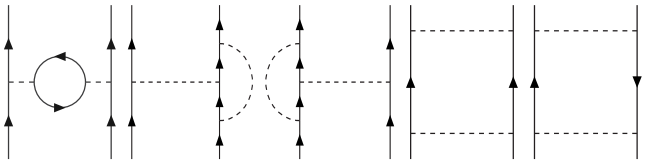

FIG. 2. Diagrams appearing at one-loop RG. Each vertex can be represented by either a 4×4 matrix (spinless) or 8×8 matrix (spin-1/2) case.

$$\begin{aligned} (\psi^\dagger C_1\psi)^2 = &-(\psi^\dagger A_1\psi)^2 + [(\psi^\dagger A_2\psi)^2 + (\psi^\dagger D_1\psi)^2] \\ &- 2(\psi^\dagger D_2\psi)^2 - [(\psi^\dagger C_3\psi)^2 + (\psi^\dagger D_3\psi)^2], \end{aligned} \tag{54}$$

$$\begin{aligned} (\psi^\dagger A_3\psi)^2 + (\psi^\dagger B_3\psi)^2 = &-2(\psi^\dagger A_1\psi)^2 - 2(\psi^\dagger D_2\psi)^2 \\ &- [(\psi^\dagger C_3\psi)^2 + (\psi^\dagger D_3\psi)^2], \end{aligned} \tag{55}$$

and

$$\begin{aligned} (\psi^\dagger B_4\psi)^2 + (\psi^\dagger A_4\psi)^2 + (\psi^\dagger C_4\psi)^2 + (\psi^\dagger D_4\psi)^2 = &-2[(\psi^\dagger A_2\psi)^2 \\ &+ (\psi^\dagger D_1\psi)^2] + 4(\psi^\dagger D_2\psi)^2 + 2[(\psi^\dagger C_3\psi)^2 + (\psi^\dagger D_3\psi)^2], \end{aligned} \tag{56}$$

in favor of the remaining four terms. These equations will be used in deriving our RG equations since elimination of fast modes will generate terms such as, for example, $(\psi^\dagger B_2\psi)^2$. The above equations show that such a term does not correspond to a new coupling in a renormalized action but rather is a linear combination of terms already present.

Finally, we arrive at our interaction Lagrangian

$$\begin{aligned} \mathcal{L}_{int} = &\frac{1}{2}\int d^2\mathbf{r}[g_{A_1}[\psi^\dagger A_1\psi(\mathbf{r},\tau)]^2 + g_{A_2}\{[\psi^\dagger A_2\psi(\mathbf{r},\tau)]^2 \\ &+ [\psi^\dagger D_1\psi(\mathbf{r},\tau)]^2\}] + \frac{1}{2}\int d^2\mathbf{r}[g_{D_2}[\psi^\dagger D_2\psi(\mathbf{r},\tau)]^2 \\ &+ g_\gamma\{[\psi^\dagger C_3\psi(\mathbf{r},\tau)]^2 + [\psi^\dagger D_3\psi(\mathbf{r},\tau)]^2\}]. \end{aligned} \tag{57}$$

Above is the most general four-fermion contact interaction Lagrangian for spinless fermions allowed by the symmetry of the A-B stacked honeycomb bilayer. In the next section, we study the weak-coupling RG flow of the four couplings g_{A_1}, g_{A_2}, g_{D_2}, and g_γ. The first three couplings appeared in our previous work[3] where we called them g_1, g_2, and g_3. The fourth coupling, g_γ, did not appear there since the starting point assumed only finite g_1 and, as we will see later, g_γ is not generated if its starting value is zero.

IV. RENORMALIZATION GROUP ANALYSIS

Clearly, g_{ST}'s are marginal by power counting and the question is how they flow. The RG procedure employed here follows Ref. 22 and consists of integrating out the fermionic modes in a thin shell between the initial cutoff Λ and Λ/s while the integral over ω extends from $-\infty$ to ∞. Since we are working in weak coupling, we can integrate out the fast modes perturbatively in g's. The diagrams needed are shown in Fig. 2. Afterward, the lengths $\mathbf{r}$, times τ and the modes ψ

are rescaled according to Eq. (32) and the change in the coupling constants is noted. (To the order we are working, the dynamical critical exponent z remains 2.) While the details of the derivation are provided in Appendix A, we note in passing that the analysis is facilitated by the use of the identities

$$\int_{-\infty}^{\infty}\frac{d\omega}{2\pi}\int_{\Lambda/s}^{\Lambda}\frac{d^2\mathbf{k}}{(2\pi)^2}G_{\mathbf{k}}(i\omega)\otimes G_{\mp\mathbf{k}}(\mp i\omega)$$
$$=\left(\pm 1_4\otimes 1_4+\frac{1}{2}\sum_{a=1}^{2}\gamma_a\otimes\gamma_a\right)\frac{m}{4\pi}\ln s, \tag{58}$$

where the noninteracting Green's function is

$$G_{\mathbf{k}}(i\omega)=(-i\omega+\Sigma\cdot d_{\mathbf{k}})^{-1}=\frac{i\omega+\Sigma\cdot d_{\mathbf{k}}}{\omega^2+\left(\frac{\mathbf{k}^2}{2m}\right)^2} \tag{59}$$

and, just as before, $d_{\mathbf{k}}^x=\frac{k_x^2-k_y^2}{2m}$, $d_{\mathbf{k}}^y=-\frac{2k_xk_y}{2m}$, $\Sigma^x=\gamma_2$, and $\Sigma^y=\gamma_1$.

Using this procedure, we find the RG equations for the four coupling constants to be

$$\frac{dg_{A_1}}{d\ln s}=-4g_{A_1}g_{A_2}\frac{m}{4\pi}, \tag{60}$$

$$\frac{dg_{A_2}}{d\ln s}=-(g_{A_1}^2-2g_{A_1}g_{A_2}+8g_{A_2}^2-2g_{A_2}g_{D_2}+g_{D_2}^2$$
$$+4(3g_{A_2}-g_{D_2})g_\gamma+6g_\gamma^2)\frac{m}{4\pi}, \tag{61}$$

$$\frac{dg_{D_2}}{d\ln s}=2(2g_{A_2}^2+2g_{A_1}g_{D_2}-6g_{A_2}g_{D_2}-2g_{D_2}^2$$
$$+8g_{A_2}g_\gamma+2g_\gamma^2)\frac{m}{4\pi}, \tag{62}$$

$$\frac{dg_\gamma}{d\ln s}=-2g_\gamma(-2g_{A_1}+2g_{A_2}+2g_\gamma)\frac{m}{4\pi}. \tag{63}$$

These equations reduce to the ones studied in Ref. 3 when we set $g_\gamma=0$ in this work and $N=2$ in Eqs. (6)–(8) of Ref. 3. Their analysis proceeds along the lines discussed in Ref. 3. We note that each RG equation corresponds to a quadratic polynomial in coupling constants. Therefore, dividing each equation by g_{A_2} (which is g_3 in the notation of Ref. 3), we obtain three equations

$$\frac{dg_{A_1}}{dg_{A_2}}=\mathcal{R}_{12}\left(\frac{g_{A_1}}{g_{A_2}},\frac{g_{D_2}}{g_{A_2}},\frac{g_\gamma}{g_{A_2}}\right), \tag{64}$$

$$\frac{dg_{D_2}}{dg_{A_2}}=\mathcal{R}_{32}\left(\frac{g_{A_1}}{g_{A_2}},\frac{g_{D_2}}{g_{A_2}},\frac{g_\gamma}{g_{A_2}}\right), \tag{65}$$

$$\frac{dg_\gamma}{dg_{A_2}}=\mathcal{R}_{42}\left(\frac{g_{A_1}}{g_{A_2}},\frac{g_{D_2}}{g_{A_2}},\frac{g_\gamma}{g_{A_2}}\right), \tag{66}$$

where

$$\mathcal{R}_{12}(x,y,z)=\frac{4x}{x^2-2x+8-2y+y^2+4(3-y)z+6z^2}, \tag{67}$$

$$\mathcal{R}_{32}(x,y,z)=-\frac{4(1+xy-3y-y^2+4z+z^2)}{x^2-2x+8-2y+y^2+4(3-y)z+6z^2}, \tag{68}$$

$$\mathcal{R}_{42}(x,y,z)=\frac{2z(-2x+2+2z)}{x^2-2x+8-2y+y^2+4(3-y)z+6z^2}. \tag{69}$$

Equations (64)–(66) are homogeneous, which means that we can instead study the flow of the coupling constant ratios

$$g_{A_2}\frac{d\frac{g_{A_1}}{g_{A_2}}}{dg_{A_2}}=-\frac{g_{A_1}}{g_{A_2}}+\mathcal{R}_{12}\left(\frac{g_{A_1}}{g_{A_2}},\frac{g_{D_2}}{g_{A_2}},\frac{g_\gamma}{g_{A_2}}\right), \tag{70}$$

$$g_{A_2}\frac{d\frac{g_{D_2}}{g_{A_2}}}{dg_{A_2}}=-\frac{g_{D_2}}{g_{A_2}}+\mathcal{R}_{32}\left(\frac{g_{A_1}}{g_{A_2}},\frac{g_{D_2}}{g_{A_2}},\frac{g_\gamma}{g_{A_2}}\right), \tag{71}$$

$$g_{A_2}\frac{d\frac{g_\gamma}{g_{A_2}}}{dg_{A_2}}=-\frac{g_\gamma}{g_{A_2}}+\mathcal{R}_{42}\left(\frac{g_{A_1}}{g_{A_2}},\frac{g_{D_2}}{g_{A_2}},\frac{g_\gamma}{g_{A_2}}\right). \tag{72}$$

Note that the right-hand side of these equations is a function of coupling constant *ratios only*, i.e., it is autonomous in the new variables $\frac{g_{A_1}}{g_{A_2}}$, $\frac{g_{D_2}}{g_{A_2}}$, and $\frac{g_\gamma}{g_{A_2}}$. We can think of the right-hand sides effectively as (highly nonlinear) β functions for the ratios. The advantage of rewriting the flow equations this way is that in this form it is easier to analyze the qualitative nature of the flow diagram. Unlike in the case where g_γ was assumed to vanish from the start,[3] in the present case the β function for g_{A_2} is not negative semidefinite. It may appear therefore, that we lose the directionality of the flow equations in the three-dimensional (3D) ratio space. This turns out not to be the case since the (ellipsoidal) region in the 3D ratio space where $dg_{A_2}/d\ln s$ changes sign is precisely the same region where the "β" functions for the ratios change sign, and so it is enough to determine the directionality of the flow of the trajectories near fixed points of the ratios, which turns out to be simple enough.

The qualitative analysis proceeds by finding the fixed points in the ratio space. There are four of them,

$$\left(\frac{g_{A_1}^*}{g_{A_2}^*},\frac{g_{D_2}^*}{g_{A_2}^*},\frac{g_\gamma^*}{g_{A_2}^*}\right)=(0,-1.085,0), \tag{73}$$

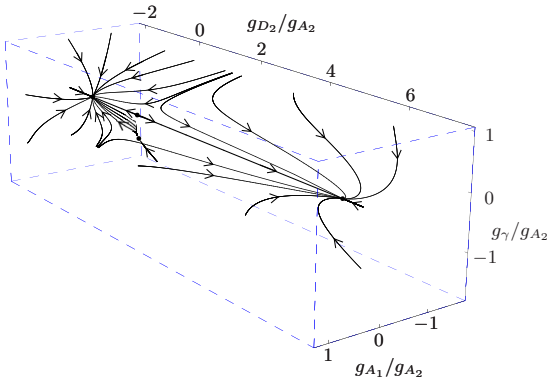

FIG. 3. (Color online) Flow diagram in the coupling constant ratio space assuming that $g_{A_2}<0$ (generic behavior). There are two sinks given by Eqs. (73) and (75) in the text and two mixed fixed ratios [Eqs. (74) and (76)]. For $g_{A_2}>0$ the flow is reversed, and generically, the divergent coupling constant ratios simply mean that g_{A_2} has shrunk and crossed 0. After this point g_{A_2} becomes negative and the directionality shown here is restored.

$$\left(\frac{g_{A_1}^*}{g_{A_2}^*},\frac{g_{D_2}^*}{g_{A_2}^*},\frac{g_\gamma^*}{g_{A_2}^*}\right)=(0,0.566,0), \tag{74}$$

$$\left(\frac{g_{A_1}^*}{g_{A_2}^*},\frac{g_{D_2}^*}{g_{A_2}^*},\frac{g_\gamma^*}{g_{A_2}^*}\right)=(0,6.519,0), \tag{75}$$

$$\left(\frac{g_{A_1}^*}{g_{A_2}^*},\frac{g_{D_2}^*}{g_{A_2}^*},\frac{g_\gamma^*}{g_{A_2}^*}\right)=(-1,-1,-1). \tag{76}$$

The first three are the $N=2$ analog of the ($N=4$) fixed ratios found in Ref. 3 while the fourth one is new. For $g_{A_2}<0$ the stability analysis gives the first [Eq. (73)] and the third one [Eq. (75)] to be sinks (see Fig. 3). The second one [Eq. (74)] is mixed, with two stable directions (negative eigenvalues) and one unstable direction (positive eigenvalue). The fourth one [Eq. (76)] is also mixed, with one positive, one negative, and one zero eigenvalues. For $g_{A_2}>0$ the directionality of the flows is reversed and the sinks become sources while the mixed fixed points remain mixed but also with reversed sense of flow. These "runaway" flows in the coupling constant ratio space for $g_{A_2}>0$ simply correspond to decrease in g_{A_2} which eventually crosses zero, where the ratios become infinite, and then become negative. Once negative, the flows are described by the two stable sinks, separated by a critical plane [3D version of the (red) separatrix shown in Fig. 3 of Ref. 3). The generic flow for initial g_{A_2} of any sign is toward large and negative g_{A_2} and toward either one of the two ratio sinks.

However, it is interesting to ask, under which (nontrivial) conditions, may all the coupling constants flow to zero. One possibility is to fine tune the initial values of g_{A_1} and g_γ to zero, set the initial value of $g_{A_2}>0$ and the ratio $-1.085 \le g_{D_2}/g_{A_2} \le 6.519$. In this case, the flow is toward both $g_{A_2}\to 0$ and $g_{D_2}\to 0$ while their ratio approaches 0.566. Note that in this case we have to fine tune two of the four symmetry allowed couplings g_{A_1} and g_γ to vanish.

Another possibility involves the new fixed point in the ratio space at $(\frac{g_{A_1}}{g_{A_2}},\frac{g_{D_2}}{g_{A_2}},\frac{g_\gamma}{g_{A_2}})=(-1,-1,-1)$. While the fixed point is mixed, in that one of the RG eigenvalues is negative and one positive, one eigenvalue, whose right eigenvector is $(\frac{1}{\sqrt{3}},\frac{1}{\sqrt{3}},\frac{1}{\sqrt{3}})$, vanishes. This means that in the vicinity of this fixed point, the flow along or against this direction in the ratio space is very slow. Importantly, our numerical integration finds that for $g_{A_2}>0$, starting *anywhere*(!) along the line $(\frac{g_{A_1}}{g_{A_2}},\frac{g_{D_2}}{g_{A_2}},\frac{g_\gamma}{g_{A_2}})=(-\lambda,-\lambda,-\lambda)$ for $0<\lambda\le 1$, the flow is toward $\lambda=1$ with *decreasing* $g_{A_2}\to 0$. The flow trajectories passing through this line segment in the ratio space, however, are *not* straight lines. In fact, they connect with the fixed point $(\frac{g_{A_1}}{g_{A_2}},\frac{g_{D_2}}{g_{A_2}},\frac{g_\gamma}{g_{A_2}})=(0,-1.085,0)$. This means that there is a nontrivial (curved) finite surface in the ratio space along which the flow is directed toward the *noninteracting* fixed point if g_{A_2} starts out positive. In this case only one parameter needs to be fine tuned in order to start on this surface. This interesting behavior, however, is nongeneric, in that such a surface is unstable, and the generic flow for initial $g_{A_2}>0$ is toward large and negative g_{A_2} and toward the two ratio sinks.

Susceptibilities and ordered states

The physics associated with the fixed ratios analyzed in the previous section can be understood by studying the flow of the susceptibilities toward forming various orders. For translationally invariant order parameters, the susceptibilities can be calculated from the above flows by introducing source terms into the action so that $S\to S+\Delta\mathcal{S}$,

$$\Delta\mathcal{S}=-\Delta_{ph}^{\mathcal{O}_i}\int d\tau d^2\mathbf{r}\,\psi^\dagger(\mathbf{r},\tau)\mathcal{O}^{(i)}\psi(\mathbf{r},\tau)$$
$$-\Delta_{pp}^{\mathcal{O}_i}\int d\tau d^2\mathbf{r}\,\psi_a(\mathbf{r},\tau)\mathcal{O}_{ab}^{(i)}\psi_b(\mathbf{r},\tau). \tag{77}$$

Next, we integrate out the fermionic modes within a small shell given by $\Lambda/s<k<\Lambda$ and find the correction to the source term perturbatively in the g's. We then substitute the flow of the g's into the prefactors of various source terms and ask which diverges the fastest as s increases.

1. Particle-hole channels

In the particle-hole channel, we therefore find

$$\Delta^{\mathcal{O}_i}(s)\psi_<^\dagger\mathcal{O}_i\psi_<(\mathbf{r},\tau)=s^2\Delta^{\mathcal{O}_i}(1)\psi_<^\dagger\mathcal{O}_i\psi_<$$
$$+s^2\Delta^{\mathcal{O}_i}(1)\sum_M g_{MM}\Pi_{\mathcal{O}M}\psi_<^\dagger M\psi_<(\mathbf{r},\tau)$$
$$-s^2\Delta^{\mathcal{O}_i}(1)\sum_M g_{MM}\psi_<^\dagger\Upsilon_{\mathcal{O}M}\psi_<(\mathbf{r},\tau), \tag{78}$$

where i is summed over the 16 independent order parameters [generators of $SU(4)$], and

$$\Pi_{\mathcal{O}M}=\int_{-\infty}^{\infty}\frac{d\omega}{2\pi}\int_{\Lambda/s}^{\Lambda}\frac{d^2\mathbf{k}}{(2\pi)^2}\mathrm{Tr}[G_{\mathbf{k}}(i\omega)\mathcal{O}_iG_{\mathbf{k}}(i\omega)M], \tag{79}$$

TABLE I. The susceptibility coefficients $\mathcal{A}_{X_j}$, $\mathcal{B}_{X_j}$, $\mathcal{C}_{X_j}$, and $\mathcal{D}_{X_j}$ in Eq. (81) for different particle-hole order parameters $\psi^\dagger \mathcal{O}_i \psi$.

$\psi^\dagger X_j \psi$	1	2	3	4
Δ_A	0, 0, 0, 0	1,−1,−4,−2	0, 0, 0, 0	1,−1,0,0
Δ_B	1,−1,0,2	0, 0, 0, 0	0, 0, 0, 0	1,−1,0,0
Δ_C	2,2,−4,−4	1,−1,0,2	2,2,−4,−8	1,−1,0,0
Δ_D	1,−1,−4,−2	1,−6,−4,4	2,2,−4,−8	1,−1,0,0

$$\Upsilon_{\mathcal{O}M} = \int_{-\infty}^{\infty} \frac{d\omega}{2\pi} \int_{\Lambda/s} \frac{d^2\mathbf{k}}{(2\pi)^2} M G_{\mathbf{k}}(i\omega) \mathcal{O}_i G_{\mathbf{k}}(i\omega) M. \quad (80)$$

Using Eq. (58) one can easily convince oneself that the only nonzero contributions to $\Pi_{\mathcal{O}M}$ come from $\mathcal{O}=M$, and that the matrix $\Upsilon_{\mathcal{O}M}$ is proportional to $\mathcal{O}$. From here we find the flow equations for the source terms

$$\frac{d \ln \Delta_{X_j}}{d \ln s} = 2 + (\mathcal{A}_{X_j} g_{A_1} + \mathcal{B}_{X_j} g_{D_2} + \mathcal{C}_{X_j} g_{A_2} + \mathcal{D}_{X_j} g_\gamma) \frac{m}{4\pi}, \quad (81)$$

where $X=A,B,C,D$ and $j=1,2,3,4$. The results of this calculation, i.e., the values of $\mathcal{A}_{X_j}$, $\mathcal{B}_{X_j}$, $\mathcal{C}_{X_j}$, and $\mathcal{D}_{X_j}$, are shown in Table I. The coupling constants g are functions of s and, in order to determine the most likely ordering tendency, it is necessary to find out which source term Δ_{X_j} grows the fastest. We can write each of these equations as

$$\frac{d \ln \Delta_{X_j}}{d \ln s} = 2 + g_{A_2} \left(\mathcal{A}_{X_j} \frac{g_{A_1}}{g_{A_2}} + \mathcal{B}_{X_j} \frac{g_{D_2}}{g_{A_2}} + \mathcal{C}_{X_j} + \mathcal{D}_{X_j} \frac{g_\gamma}{g_{A_2}} \right) \frac{m}{4\pi} \quad (82)$$

and near the two sinks, we can take $g_{A_2}<0$ and substitute the fixed point ratios.

Near the first sink $(\frac{g^*_{A_1}}{g^*_{A_2}}, \frac{g^*_{D_2}}{g^*_{A_2}}, \frac{g^*_\gamma}{g^*_{A_2}}) = (0,-1.085,0)$ and, plugging in these values, we find that the fastest divergence appears for $\Delta_{ph}^{C_1}$, $\Delta_{ph}^{C_3}$, and $\Delta_{ph}^{D_3}$. Discriminating between the first and the last two ordering tendencies requires knowledge of the sign of the subleading ratio $\frac{g_\gamma}{g_{A_2}}$.

If $\frac{g_\gamma}{g_{A_2}}<0$, i.e., if it approaches 0 from below as s increases, then the most dominant particle-hole ordering tendency is toward a finite expectation value of $C_1=\gamma_0=1_2\sigma_z$. Physically, this order parameter, which corresponds to an imbalance in the number of particles on the two different layers, opens up a gap at the **K** and **−K** points in the Brillouin zone and the system is a (trivial) insulator. As shown below, this turns out to be the case for a lattice model with a nearest-neighbor repulsion V.

On the other hand, if $\frac{g_\gamma}{g_{A_2}}>0$ and approaches zero from above as s increases, then the most dominant ordering tendency among the particle-hole channels studied here is toward finite expectation values of $C_3=\gamma_3=\tau^x\sigma^y$ and $D_3=\gamma_5=\tau^y\sigma^y$, both of which are odd under time-reversal symmetry [Eq. (40)].

Near the second sink $(\frac{g^*_{A_1}}{g^*_{A_2}}, \frac{g^*_{D_2}}{g^*_{A_2}}, \frac{g^*_\gamma}{g^*_{A_2}}) = (0,6.519,0)$ the most dominant ordering tendency is toward a finite expectation value of $D_2=i\gamma_1\gamma_2=\tau^z\sigma^z$. The corresponding order parameter also opens up a gap in the single-particle spectrum but unlike C_1, it breaks time-reversal symmetry. This results in an *anomalous quantum Hall state*, with zero B-field Hall conductivity $\sigma_{xy}=\pm 2\frac{e^2}{h}$. Such a state is a bilayer analog of the Haldane model for the quantum Hall effect without Landau levels.[24]

2. Particle-particle channels

Since our Fermions are spinless, if the integral

$$\int d^2\mathbf{r}\, \psi_a(\mathbf{r},\tau) \mathcal{O}^{(i)}_{ab} \psi_b(\mathbf{r},\tau)$$

is to be finite, we must have $\mathcal{O}^i_{ab}=-\mathcal{O}^i_{ba}$. Of the 16 $SU(4)$ generators [Eq. (42)] this condition selects the six matrices B_3, B_4, C_2, C_3, D_1, and D_4. Integrating out the fast modes, we are left with the following renormalization of the source term for the slow modes $\psi_<$:

$$\begin{aligned}
&\Delta^{\mathcal{O}_i}(s) \psi^<_a(\mathbf{r},\tau) \mathcal{O}^{(i)}_{ab} \psi^<_b(\mathbf{r},\tau) \\
&\quad = s^2 \Delta^{\mathcal{O}_i}(1) \psi^<_a(\mathbf{r},\tau) \mathcal{O}^{(i)}_{ab} \psi^<_b(\mathbf{r},\tau) \\
&\quad + s^2 \Delta^{\mathcal{O}_i}(1) \sum_M g_{MM} \int \frac{d\omega}{2\pi} \int_{\Lambda/s} \frac{d^2\mathbf{k}}{(2\pi)^2} \mathcal{O}^i_{\alpha\beta} G_{\mathbf{k},\beta a}(i\omega_n) \\
&\quad \times M_{ab} \psi_{b<}(\mathbf{r},\tau) G_{-\mathbf{k},\alpha c}(i\omega_n) M_{cd} \psi_{d<}(\mathbf{r},\tau). \quad (83)
\end{aligned}$$

Evaluating the necessary matrix products leads to

$$\frac{d \ln \Delta_{B_3}}{d \ln s} = 2 - (g_{A_1} + g_{D_2} - 2g_\gamma) \frac{m}{4\pi}, \quad (84)$$

$$\frac{d \ln \Delta_{B_4}}{d \ln s} = 2 - (2g_{A_1} - 2g_{D_2} + 4g_{A_2} + 4g_\gamma) \frac{m}{4\pi}, \quad (85)$$

$$\frac{d \ln \Delta_{C_3}}{d \ln s} = 2 - (g_{A_1} + g_{D_2} - 2g_\gamma) \frac{m}{4\pi}, \quad (86)$$

$$\frac{d \ln \Delta_{C_2}}{d \ln s} = \frac{d \ln \Delta_{D_1}}{d \ln s} = \frac{d \ln \Delta_{D_4}}{d \ln s} = 2. \quad (87)$$

Near the first sink $(\frac{g^*_{A_1}}{g^*_{A_2}}, \frac{g^*_{D_2}}{g^*_{A_2}}, \frac{g^*_\gamma}{g^*_{A_2}}) = (0,-1.085,0)$ and, substituting these values into Eqs. (84)–(87), we find that the strongest divergence appears for $\Delta_{pp}^{B_4}$. The *leading* divergence is as fast as for $\Delta_{ph}^{C_1}$, $\Delta_{ph}^{C_3}$, and $\Delta_{ph}^{D_3}$ but it differs in the subleading terms. In fact, for $g_{A_1}>0$, the strongest divergence is in the particle-hole channel $\Delta_{ph}^{C_1}$ discussed above. In principle, fine tuning and keeping the subleading term $g_{A_1}/g_{A_2}<0$ (and setting $g_\gamma=0$ or keeping $g_\gamma/g_{A_2}<0$) may lead to the strongest divergence appearing in the particle-particle channel.

V. t-V MODEL FOR SPINLESS FERMIONS

While the weak-coupling results are quite general, we can apply them to a specific microscopic model, which happens

to be quite revealing in that we can also analyze it for strong coupling and thus compare the two regimes. We consider spinless fermions hopping on the half-filled A-B stacked honeycomb bilayer, with nearest-neighbor hoppings t and $t_\perp$ only and with nearest-neighbor repulsions V and $V_\perp$. The corresponding Hamiltonian is

$$\mathcal{H} = H_0^\perp + H_0^\parallel + \mathcal{V}^\perp + \mathcal{V}^\parallel, \tag{88}$$

where

$$H_0^\perp = -t_\perp \sum_{\mathbf{R}} [a_1^\dagger(\mathbf{R}) a_2(\mathbf{R}) + \text{H.c.}],$$

$$H_0^\parallel = -t \sum_{\mathbf{R},\delta} [b_1^\dagger(\mathbf{R}+\delta) a_1(\mathbf{R}) + b_2^\dagger(\mathbf{R}-\delta) a_2(\mathbf{R}) + \text{H.c.}], \tag{89}$$

$$\mathcal{V}^\perp = V_\perp \sum_{\mathbf{R}} \left[a_1^\dagger(\mathbf{R}) a_1(\mathbf{R}) - \frac{1}{2} \right] \left[a_2^\dagger(\mathbf{R}) a_2(\mathbf{R}) - \frac{1}{2} \right],$$

$$\mathcal{V}^\parallel = V \sum_{\mathbf{R},\delta} \left[a_1^\dagger(\mathbf{R}) a_1(\mathbf{R}) - \frac{1}{2} \right] \left[b_1^\dagger(\mathbf{R}+\delta) b_1(\mathbf{R}+\delta) - \frac{1}{2} \right] + V \sum_{\mathbf{R},\delta} \left[a_2^\dagger(\mathbf{R}) a_2(\mathbf{R}) - \frac{1}{2} \right] \left[b_2^\dagger(\mathbf{R}-\delta) b_2(\mathbf{R}-\delta) - \frac{1}{2} \right]. \tag{90}$$

A. Weak coupling

In order to project onto the low-energy modes, we first rewrite Hamiltonian (88) as an imaginary time Grassman path integral. We then integrate out the a_1 and a_2 modes perturbatively. This results in

$$\mathcal{L}_{eff}^{(t-V)} = \mathcal{L}_0 + \mathcal{L}_{int}, \tag{91}$$

where

$$\mathcal{L}_0 = \frac{t^2}{t_\perp} \sum_{\mathbf{R},\delta,\delta'} [b_1^\dagger(R+\delta,\tau) b_2(R-\delta',\tau) + \text{H.c.}], \tag{92}$$

$$\mathcal{L}_{int} = -\frac{V^2}{8t_\perp} \sum_{\mathbf{R}} \left[\sum_\delta n_{b_1}(\mathbf{R}+\delta,\tau) - n_{b_2}(\mathbf{R}-\delta,\tau) \right]^2. \tag{93}$$

Fourier transforming the Fermi modes in the first term [Eq. (92)] gives rise to the kinetic-energy term [Eq. (24)] with $m = 2t_\perp/(9t^2)$. The interaction term can be written as

$$\mathcal{L}_{int} = -\frac{V^2}{8t_\perp} \frac{1}{N_{uc}} \sum_{\mathbf{q},\mathbf{G}} \{ [d_{-\mathbf{q}} n_{b_1,-\mathbf{q}}(\tau) - d_{\mathbf{q}} n_{b_2,-\mathbf{q}}(\tau)] \times [d_{\mathbf{q}+\mathbf{G}} n_{b_1,\mathbf{q}+\mathbf{G}}(\tau) - d_{\mathbf{G}-\mathbf{q}} n_{b_2,\mathbf{G}+\mathbf{q}}(\tau)] \}, \tag{94}$$

where $\mathbf{G}$ is a reciprocal lattice vector and $n_{b_{j,\mathbf{q}}} = \frac{1}{N_{uc}} \Sigma_{\mathbf{k}} b_{j,\mathbf{k}}^\dagger b_{j,\mathbf{k}+\mathbf{q}}$. In addition, each fermionic mode is restricted to reside in the first Brillouin zone. Taking $\mathbf{k}$ in the above sum to be near $\mathbf{K}$ or $-\mathbf{K}$ gives two possibilities for $\mathbf{q}$: either $\mathbf{q} \sim 0$ or $\mathbf{q} \sim \pm 2\mathbf{K}$. Note that in the first case $d_0 = 3$ while in the second case $d_{\pm 2\mathbf{K}} = 0$. Therefore, only the first term contributes a marginal coupling, and the above Hamiltonian gives rise to the low-energy interaction Lagrangian

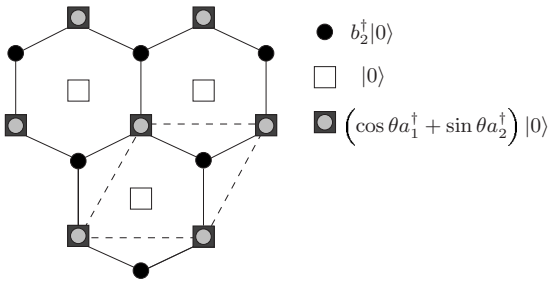

FIG. 4. Schematic representation of the strong-coupling state for the spinless t-V model. For $t=0$ but finite $t_\perp$, V, and $V_\perp$, the sublattice b_1 is empty, while sublattice b_2 is fully occupied. The a_1-a_2 dimer is singly occupied, with an electron partially *delocalized* onto a_2 despite the repulsion from the occupied b_2 sites. Such gapped state breaks inversion symmetry between the layers 1 and 2.

$$\mathcal{L}_{int}^{t-V} = g_{C_1}^{(0)} \int d^2\mathbf{r} [\psi^\dagger C_1 \psi(\mathbf{r},\tau)]^2, \tag{95}$$

where

$$g_{C_1}^{(0)} = -\frac{9V^2}{8t_\perp} A_{uc}^{-1}. \tag{96}$$

The area of the unit cell $A_{uc} = \hat{z} \cdot (\mathbf{R}_1 \times \mathbf{R}_2) = \frac{3\sqrt{3}}{2} a^2$. This means that we should start our RG flow with a small and negative (attractive) $g_{C_1}^{(0)} (\psi^\dagger C_1 \psi)^2$, which should be rewritten using the Fierz identity [Eq. (54)]. The initial conditions are therefore

$$g_{A_1}(s=1) = -g_{C_1}^{(0)}, \quad g_{D_2}(s=1) = -2g_{C_1}^{(0)}, \tag{97}$$

$$g_{A_2}(s=1) = g_{C_1}^{(0)}, \quad g_\gamma(s=1) = -g_{C_1}^{(0)}. \tag{98}$$

Substituting these as the initial conditions into our RG equations we find that none of the coupling constants change sign and they all diverge at the same value of s. The ratios of the couplings flow to the fixed point $(\frac{g_{A_1}^*}{g_{A_2}^*}, \frac{g_{D_2}^*}{g_{A_2}^*}, \frac{g_\gamma^*}{g_{A_2}^*}) = (0, -1.085, 0)$. Therefore, as discussed in the previous section, the fastest divergence appears in the channel $1_2\sigma_z$. We therefore conclude that the weak-coupling instability of this model is toward a gapped, broken inversion symmetry state with an imbalance of the number of particles on layer 1 compared to layer 2 (Fig. 4).

B. Strong-coupling limit

Setting $t = t_\perp = 0$ we find three ground states at half filling: (i) each site of sublattice a_1 and of b_2 is singly occupied, (ii) each site of sublattice a_2 and of b_1 is singly occupied, and (iii) each site of sublattice b_1 and of b_2 is singly occupied. Each of these states breaks sublattice symmetry but the average density of particles on each layer is the same and equal

to 1 per unit cell (which contains two sites in each layer). The states (i) and (ii) differ from the state (iii) by the occupation of the a_1-a_2 dimer which is singly occupied for the former and empty for the latter.

If we now set $t=0$ but $t_\perp \neq 0$ then we can further lower the energy of (i) and (ii) by delocalizing the electron on the dimer. So, consider the deformation of the state (i): we seek a state of the form

$$|\Psi_\theta\rangle = \prod_{\mathbf{R}} [\cos\,\theta a_1^\dagger(\mathbf{R}) + \sin\,\theta a_2^\dagger(\mathbf{R})] b_2^\dagger(\mathbf{R}+\delta)|0\rangle. \quad (99)$$

For $t_\perp = 0$, we have $\theta = 0$ but once $t_\perp \neq 0$ we expect $\theta \neq 0$.

Acting on $|\Psi_\theta\rangle$ with $\mathcal{H}$ (for $t=0$) and requiring $|\Psi_\theta\rangle$ to be an eigenstate gives

$$\left(-\frac{V_\perp}{4} - \frac{3V}{2}\right)\cos\,\theta - t_\perp \sin\,\theta = E\cos\,\theta, \quad (100)$$

$$-t_\perp \cos\,\theta + \left(-\frac{V_\perp}{4} + \frac{3V}{2}\right)\cos\,\theta = E\sin\,\theta. \quad (101)$$

The above equation has two eigenvalues $E_\pm = -\frac{V_\perp}{4} \pm \sqrt{t_\perp^2 + \frac{9V^2}{4}}$, and clearly $t_\perp$ favors a state with a delocalized particle on the dimer. Thus in the ground state

$$\cos\,\theta = \frac{1}{\sqrt{2}}\sqrt{1 + \frac{3V}{2\left(E_+ + \frac{V_\perp}{4}\right)}}, \quad (102)$$

$$\sin\,\theta = \frac{1}{\sqrt{2}}\sqrt{1 - \frac{3V}{2\left(E_+ + \frac{V_\perp}{4}\right)}}. \quad (103)$$

This state breaks the sublattice symmetry and there are clearly more particles on layer 2 than on layer 1. Similarly, if we deform (ii) in analogous way, we will find a state with more particles on layer 1 than on layer 2. Both of these states are gapped.

For infinitesimal t, we expect the energy of the broken symmetry state to be further lowered via second-order processes. This leads us to the conclusion that in the strong-coupling limit, our Hamiltonian $\mathcal{H}$ has a ground state with broken inversion symmetry, i.e., the total number of particles on the upper layer is different from the total number of particles on the lower layer.

VI. SPIN-$\frac{1}{2}$ CASE

The symmetry-based reduction in the number of coupling can be used for the spin-$\frac{1}{2}$ case as well. All the arguments presented in the section dealing with short range interactions follow through but now the Fierz vector is 18 dimensional, instead of 9. Specifically, each term in Eq. (49), when multiplied by the appropriate coupling, gives rise to two terms as

$$g_{X_j}(\psi^\dagger X_j \psi)^2 \to g_{X_j}^{(c)}(\psi_\alpha^\dagger X_j \psi_\alpha)^2 + g_{X_j}^{(s)}(\psi_\alpha^\dagger X_j \vec{\sigma}_{\alpha\beta}\psi_\beta)^2, \quad (104)$$

where the Pauli $\vec{\sigma}$ corresponds to spin-$\frac{1}{2}$ $SU(2)$. The seemingly independent couplings in the two different channels, c and s, are still related to each other via a Fierz-type identity.

In particular, we can use the $SU(8)$ algebraic identity

$$S_{ij}T_{mn} = \frac{1}{64}\mathrm{Tr}[S\Lambda^a T\Lambda^b]\Lambda^b_{in}\Lambda^a_{mj}, \quad (105)$$

where S and T are 8×8 matrices, and the 64 generators Λ^a can be obtained from the 16 $SU(4)$ generators as $\{\Gamma^a \otimes 1, \Gamma^a \otimes \sigma^z, \Gamma^a \otimes \sigma^x, \Gamma^a \otimes \sigma^y\}$. This leads to

$$[\psi^\dagger(x)S\psi(x)][\psi^\dagger(y)T\psi(y)] = -\frac{1}{64}\mathrm{Tr}[S\Lambda^a T\Lambda^b][\psi^\dagger(x)\Lambda^b\psi(y)] \times [\psi^\dagger(y)\Lambda^a\psi(x)]. \quad (106)$$

Again, the minus sign comes from ψ and $\psi^\dagger$ being anticommuting (four component) Grassman fields. For contact terms $x=y$ and the above equation constitutes a set of linear relations among the 18 symmetry allowed terms.

If we now arrange the quartic terms into an 18-component vector $\mathcal{V}$ [Eq. (B1)] we can write the above constraint as

$$\mathcal{F}\mathcal{V} = 0, \quad (107)$$

where the matrix $\mathcal{F}$, displayed in Appendix B [Eq. (B2)], has nine zero eigenvalues, and, as a result[17] there are nine independent couplings in the spin-$\frac{1}{2}$ case. From here it can be shown that one can eliminate *all* the (spin-spin) g_X^s couplings in favor of the (charge-charge) g_X^c couplings.[6]

Using the same technique as described for the spinless case in Appendix A, we find the RG flow equations for the nine couplings in the spin-1/2 case. These equations, (A10)–(A17), are shown explicitly at the end of Appendix A. While full analysis of Eqs. (A10)–(A17) is beyond the scope of this paper, we have studied the effect of three of these couplings in Ref. 3, starting with $g_{A_1}^{(c)}$, and generating $g_{A_2}^{(c)}$ and $g_{D_2}^{(c)}$. No other couplings are generated, assuming they vanish to begin with, in agreement with Eqs. (A10)–(A17). The equations presented in Appendix A of this paper reduce to Eqs. (6)–(8) of Ref. 3 provided we set $N=4$ there and identify $g_1 \leftrightarrow g_{A_1}^{(c)}$, $g_2 \leftrightarrow g_{D_2}^{(c)}$, and $g_3 \leftrightarrow g_{A_2}^{(c)}$. In this case, for finite initial $g_{A_1}^{(c)} > 0$ and vanishing initial $g_{A_2}^{(c)}$ and $g_{D_2}^{(c)}$, the most dominant divergence appears in the nematic channel, which corresponds to one of the ratio sinks $g_{D_2}^{*(c)}/g_{A_2}^{*(c)} = m_1 \approx -0.525$. For certain combinations of the couplings, a different sink $(g_{D_2}^{*(c)}/g_{A_2}^{*(c)} = m_3 \approx 13.98$, top fixed point in Fig. 3 in Ref. 3) may be reached. Thus, an anomalous quantum Hall state may in principle be stabilized in weak coupling as well. Finally, we note in passing that the number [Eq. (9)] of independent couplings in the spin-$\frac{1}{2}$ case is in agreement with Ref. 6 but disagreement with Ref. 4.

Susceptibilities

Just as in the spinless case we can analyze the flow of various source terms Δ in order to determine the most dominant weak-coupling ordering tendencies. Since in the spin-1/2 case there are nine independent coupling constants, we have

TABLE II. The susceptibility coefficients (spin-1/2 case) $\mathcal{A}_{X_j}$, $\mathcal{B}_{X_j}$, $\mathcal{C}_{X_j}$, $\mathcal{D}_{X_j}$, $\mathcal{E}_{X_j}$, $\mathcal{F}_{X_j}$, $\mathcal{G}_{X_j}$, $\mathcal{H}_{X_j}$, and $\mathcal{I}_{X_j}$ in Eq. (81) for different particle-hole order parameters $\psi^\dagger \mathcal{O}_i \psi$.

$\psi^\dagger X_j \otimes 1 \psi$	1	2	3	4
Δ_A	0, 0, 0, 0, 0, 0, 0, 0, 0	1,−1,−8,−2,0,1,−1,2,0	0, 0, 0, 0, 0, 0, 0, 0, 0	1,−1,0,0,0,−1,1,0,−8
Δ_B	1,−1,0,2,−8,1,−1,−2,0	0, 0, 0, 0, 0, 0, 0, 0, 0	0, 0, 0, 0, 0, 0, 0, 0, 0	1,−1,0,0,0,−1,1,0,−8
Δ_C	2,2,−4,−4,−4,2,−14,−4,8	1,−1,0,2,−8,1,−1,−2,0	2,2,−4,−16,4,−2,−2,0,0	1,−1,0,0,0,−1,1,0,−8
Δ_D	1,−1,−8,−2,0,1,−1,2,0	2,−14,−4,4,−4,2,2,4,−8	2,2,−4,−16,4,−2,−2,0,0	1,−1,0,0,0,−1,1,0,−8
$\psi^\dagger X_j \otimes \vec{\sigma} \psi$	1	2	3	4
Δ_A	0, 0, 0, 0, 0, 0, 0, 0, 0	1,−1,0,−2,0,1,−1,2,0	0, 0, 0, 0, 0, 0, 0, 0, 0	1,−1,0,0,0,−1,1,0,0
Δ_B	1,−1,0,2,0,1,−1,−2,0	0, 0, 0, 0, 0, 0, 0, 0, 0	0, 0, 0, 0, 0, 0, 0, 0, 0	1,−1,0,0,0,−1,1,0,0
Δ_C	2,2,−4,−4,−4,2,2,−4,8	1,−1,0,2,0,1,−1,−2,0	2,2,−4,0,4,−2,−2,0,0	1,−1,0,0,0,−1,1,0,0
Δ_D	1,−1,0,−2,0,1,−1,2,0	2,2,−4,4,−4,2,2,4,−8	2,2,−4,0,4,−2,−2,0,0	1,−1,0,0,0,−1,1,0,0

$$\frac{d \ln \Delta_{X_j}}{d \ln s} = 2 + (\mathcal{A}_{X_j} g_{A_1} + \mathcal{B}_{X_j} g_{D_2} + \mathcal{C}_{X_j} g_{A_2} + \mathcal{D}_{X_j} g_\gamma + \mathcal{E}_{X_j} g_{B_1} + \mathcal{F}_{X_j} g_{B_2} + \mathcal{G}_{X_j} g_{C_1} + \mathcal{H}_{X_j} g_\alpha + \mathcal{I}_{X_j} g_\beta) \frac{m}{4\pi}. \quad (108)$$

The coefficients $\mathcal{A}$–$\mathcal{I}$ in 32 different particle-hole channels are listed in Table II. The most dominant instability channel, X_j, yields the largest right-hand side of the above equation (Fig. 5).

VII. HUBBARD MODEL ON THE *A-B* STACKED HONEYCOMB BILAYER

In this section we use the above machinery to study the weak- and strong-coupling limits of the repulsive Hubbard model on the *A-B* stacked honeycomb bilayer. Just as before, we assume nearest-neighbor hopping only, and the potential energy term can be written as

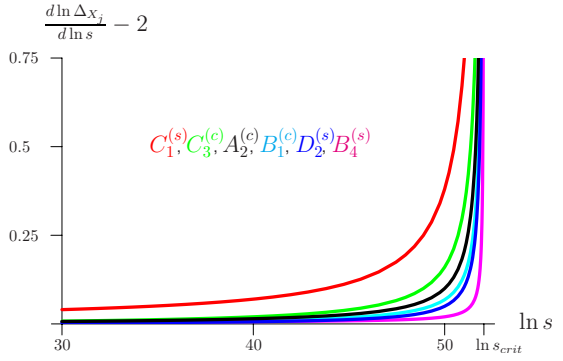

FIG. 5. (Color online) Susceptibility vs $\ln s$ [Eq. (108)] for the Hubbard model with initial $\frac{m}{4\pi A_c} U = 0.01$, in the channels $C_1^{(s)}$–$B_4^{(s)}$ (left to right). The fastest divergence appears in the antiferromagnetic channel $C_1 \otimes \vec{\sigma}$. Altogether 32 particle-hole channels have been analyzed (Table II); the channels not shown are either symmetry related to the ones shown, or $d \ln \Delta / d \ln s - 2$ vanishes (or is negative).

$$\mathcal{V}^{(H)} = U \sum_{j=1}^{2} \sum_{\mathbf{R}} a_{j\uparrow}^\dagger(\mathbf{R}) a_{j\uparrow}(\mathbf{R}) a_{j\downarrow}^\dagger(\mathbf{R}) a_{j\downarrow}(\mathbf{R}) + U \sum_{\mathbf{R}} b_{1\uparrow}^\dagger(\mathbf{R} + \delta) b_{1\uparrow}(\mathbf{R} + \delta) b_{1\downarrow}^\dagger(\mathbf{R} + \delta) b_{1\downarrow}(\mathbf{R} + \delta) + U \sum_{\mathbf{R}} b_{1\uparrow}^\dagger(\mathbf{R} - \delta) b_{1\uparrow}(\mathbf{R} - \delta) b_{1\downarrow}^\dagger(\mathbf{R} - \delta) b_{1\downarrow}(\mathbf{R} - \delta). \quad (109)$$

A. Weak-coupling limit

Projecting the Hubbard interaction onto the low energy modes we find

$$\mathcal{L}_{int} = \frac{U}{2A_{uc}} \sum_{j=1}^{2} \int d^2\mathbf{r} [(\psi^\dagger \mathcal{M}_j^{(f)} \psi)(\psi^\dagger \mathcal{M}_j^{(f)} \psi) + (\psi^\dagger \mathcal{M}_j^{(b)} \psi) \times (\psi^\dagger \mathcal{M}_j^{(b)^T} \psi) + (\psi^\dagger \mathcal{M}_j^{(b)^T} \psi)(\psi^\dagger \mathcal{M}_j^{(b)} \psi)], \quad (110)$$

where

$$\mathcal{M}_1^{(f)} = \begin{pmatrix} 1 & 0 & 0 & 0 \\ 0 & 0 & 0 & 0 \\ 0 & 0 & 1 & 0 \\ 0 & 0 & 0 & 0 \end{pmatrix} \otimes 1_2, \quad \mathcal{M}_2^{(f)} = \begin{pmatrix} 0 & 0 & 0 & 0 \\ 0 & 1 & 0 & 0 \\ 0 & 0 & 0 & 0 \\ 0 & 0 & 0 & 1 \end{pmatrix} \otimes 1_2,$$

$$\mathcal{M}_1^{(b)} = \begin{pmatrix} 0 & 0 & 1 & 0 \\ 0 & 0 & 0 & 0 \\ 0 & 0 & 0 & 0 \\ 0 & 0 & 0 & 0 \end{pmatrix} \otimes 1_2, \quad \mathcal{M}_2^{(b)} = \begin{pmatrix} 0 & 0 & 0 & 0 \\ 0 & 0 & 0 & 1 \\ 0 & 0 & 0 & 0 \\ 0 & 0 & 0 & 0 \end{pmatrix} \otimes 1_2.$$

The eight-component Fermi fields ψ are understood to be at space-(imaginary-)time point $\mathbf{r}$, τ.

Using the notation established in the previous sections, we note that the above interaction terms in the low energy effective Lagrangian can be written as

$$\mathcal{L}_{int} = \frac{U}{4A_{uc}} \int d^2\mathbf{r} \Big[(\psi^\dagger A_1 \otimes 1\psi)^2 + (\psi^\dagger C_1 \otimes 1\psi)^2 + \frac{1}{2} \sum_{X=A,B,C,D} (\psi^\dagger X_4 \otimes 1\psi)^2 \Big]. \quad (111)$$

This means that, of the nine symmetry-allowed coupling constants, the only nonzero ones are $g_{A_1}^{(c)}$, $g_{C_1}^{(c)}$, and $g_\beta^{(c)}$, with initial values

$$g_{A_1}^{(c)}(s=1) = g_{C_1}^{(c)}(s=1) = \frac{U}{4A_{uc}}, \quad (112)$$

$$g_\beta^{(c)}(s=1) = \frac{U}{8A_{uc}}. \quad (113)$$

Next, we numerically solve the RG flow [Eqs. (A10)–(A17)] with the above initial conditions [for $mU/(4\pi A_{uc})=0.01$], and substitute the resulting s-dependent couplings into the susceptibility flow [Eq. (108)] using the coefficients displayed in Table II. Comparison of the resulting susceptibilities in 32 particle-hole channels shows that the most dominant divergence appears for $\mathcal{O}=C_1\otimes\vec{\sigma}$. Physically, this corresponds to an antiferromagnetic state, with antialigned spins on the sites b_1 and b_2.

B. Strong coupling

It is well known that[25] in the strong-coupling limit $U/t \gg 1$ the Hubbard model with one particle per site is equivalent to the spin-1/2 Heisenberg model with antiferromagnetic coupling $J \sim t^2/U$. If we set $t_\perp = 0$, the two honeycomb layers decouple and at strong coupling each layer orders antiferromagnetically[26] with a sublattice magnetization that is free to point along any direction on each layer. Once $t_\perp$ is finite, the sublattice magnetizations on the two different layers lock into relative antiferromagnetic arrangement. We thus find that the half-filled Hubbard model on the A-B stacked honeycomb bilayer orders antiferromagnetically in both the weak- and strong-coupling limits.

VIII. CONCLUSIONS

We have studied the effect of short-range interactions on fermions moving on the A-B stacked bilayer. In order to access the "strong-coupling phases"[9] from weak coupling, we have fine tuned the spectrum of the noninteracting Hamiltonian to achieve parabolic degeneracy, with the ensuing logarithmically divergent susceptibilities that appear in several channels. We have found that, in the spinless fermion case, the typical dominant ordering tendency opens a spectral gap, although the nature of the resulting insulating state may be dramatically different. For example, the weak-coupling limit of the spinless t-V model, with nearest-neighbor hopping and nearest-neighbor repulsion, leads to an inversion symmetry-breaking (trivial) insulating phase while the (right) sink in the RG flow diagram shown in Fig. 3 corresponds to a spontaneously time-reversal symmetry-breaking anomalous quantum Hall phase with $\sigma_{xy} = \pm 2e^2/h$. Under certain conditions, the dominant instability may appear in the particle-particle channel as well. In addition to the generic instabilities of the spinless model, fine tuning of the initial couplings may lead to a flow toward the noninteracting fixed point. While such behavior is nongeneric, it is interesting that there is an entire surface in the ratio space (Fig. 3) which gives rise to such a flow for positive initial g_{A_2}. We have also studied the strong-coupling limit of the t-V model. In this case, the ground-state wave function can be shown to explicitly display inversion symmetry breaking. Since the same type of order is found in the asymptotic limits of strong and weak couplings, it is reasonable to assume that for this specific model, such ordering happens for any (repulsive) coupling strength.

In the spin-1/2 case, we find nine independent, symmetry-allowed couplings, and their RG flow equations. While these equations have not been studied in their entirety, they reduce to the ones presented before in Ref. 3, in which case an analysis similar to the one presented for the spinless case here, leads to either a nematic phase or an anomalous quantum Hall phase with $\sigma_{xy} = \pm 4e^2/h$, where the extra factor of 2 compared to the spinless case is due to trivial spin degeneracy.

Moreover, these Eqs. (A10)–(A17) are solved numerically for the spin-1/2 Hubbard model at half filling. The initial values of the effective couplings are such that the most dominant particle-hole instability appears in the antiferromagnetic channel. This dominance has been established by comparing susceptibilities toward 32 different ordering tendencies. Since the same instability appears in the strong-coupling limit, it is reasonable to conclude that the antiferromagnetic order sets in for any $U>0$.

When trigonal warping, which at the noninteracting level results in splitting of the parabolic degeneracy into four Dirac points, is taken into account, the logarithmic infrared divergences are cut off[3,6] by the energy scale associated with the deviation from the parabolic spectrum. This means that the noninteracting system is stable toward *infinitesimal* coupling, i.e., there are no true weak-coupling instabilities. The RG equations derived in this work will still hold down to either the energy scale associated with the divergence of the coupling constants/susceptibilities or to the energy scale associated with deviations from parabolic spectrum. In the former case the transition into broken symmetry states predicted here will occur even if the trigonal warping effects are not explicitly a part of the analysis. In the latter case, the values of the couplings obtained at the scale where deviations from parabolic spectrum must be included should be used as the initial values for a new set of RG equations associated with four Dirac points. Since Dirac points are stable toward *infinitesimal* short range interactions, the starting renormalized values of the couplings must exceed some, yet not accurately known, critical value. It is in this sense that true weak-coupling (particle-hole) instabilities disappear in the absence of fine tuning. Nevertheless, this critical value is expected to scale with energy scale associated with the van Hove singularities, and so should be appreciably smaller than in the single-layer graphene.

It is also worth noting that no such fine tuning is necessary for the models with parabolic touching studied in Ref. 8 in which case there are true weak-coupling instabilities. Unfortunately, one cannot just immediately translate the results regarding the dominance and the nature of the weak-coupling broken symmetry states found here for the honeycomb bilayer because (1) the location of the degenerate points in the Brillouin zone is (qualitatively) different and (2) the lattice symmetry will, in general, allow different contact terms than those found here.

ACKNOWLEDGMENTS

This work was supported in part by NSF CAREER award under Grant No. DMR-0955561. I also wish to thank the Aspen Center for Physics, where parts of this work were completed, for hospitality.

APPENDIX A: DETAILS OF THE RG DERIVATION

For general coupling constants g_{ST}, expanding in powers of g, gives the cumulant expansion

$$\left\langle e^{-(1/2)g_{ST}\int_1 \psi^\dagger S\psi\psi^\dagger T\psi(1)}\right\rangle \approx e^{-(1/2)g_{ST}\langle\int_1 \psi^\dagger S\psi\psi^\dagger T\psi(1)\rangle}\times\exp\left[\frac{g_{ST}g_{UV}}{8}\int_{1,2}\{\langle[\psi^\dagger S\psi\psi^\dagger T\psi(1)][\psi^\dagger U\psi\psi^\dagger V\psi(2)]\rangle-\langle[\psi^\dagger S\psi\psi^\dagger T\psi(1)]\rangle\times\langle[\psi^\dagger U\psi\psi^\dagger V\psi(2)]\rangle\}\right],$$

where the average $\langle\cdots\rangle$ is with respect to the Gaussian weighting factor. We have used a short-hand 1,2 for the modes at the space (imaginary) time $\tau_{1,2}$ and $\mathbf{r}_{1,2}$ and each $\psi=\psi_>+\psi_<$. We integrate over the fast modes $\psi_>$ whose wave numbers $\Lambda/s<k<\Lambda$. The noninteracting Green's function is

$$G_{\mathbf{k}}(i\omega)=(-i\omega+\Sigma\cdot d_{\mathbf{k}})^{-1}=\frac{i\omega+\Sigma\cdot d_{\mathbf{k}}}{\omega^2+\left(\frac{\mathbf{k}^2}{2m}\right)^2} \tag{A1}$$

and just as before $d^x_{\mathbf{k}}=\frac{k_x^2-k_y^2}{2m}$, $d^y_{\mathbf{k}}=-\frac{2k_xk_y}{2m}$, and, in the spinless case, $\Sigma^x=\gamma_2$ and $\Sigma^y=\gamma_1$.

Using the identities [Eq. (58)], we can evaluate the needed diagrams. All possible contractions correspond to the diagrams in Fig. 2.

For the first diagram we find the following terms:

$$\Delta S^{(\mathrm{RPA})}_{eff}=\frac{1}{2}\sum_{S\in\mathcal{G}}\sum_{U\in\mathcal{G}}g_Sg_U\int_1\int_2\psi^\dagger(1)S\psi(1)\times\mathrm{Tr}[SG(1-2)UG(2-1)]\psi^\dagger(2)U\psi(2), \tag{A2}$$

where, in the spinless case, $\mathcal{G}=\{A_1,A_2,D_1,D_2,C_3,D_3\}$ and the corresponding couplings, in order of appearance of S in $\mathcal{G}$, are $\{g_{A_1},g_{A_2},g_{A_2},g_{D_2},g_\gamma,g_\gamma\}$. Using the gradient expansion to determine the RG fate of the marginal couplings, we find that

$$\Delta S^{(\mathrm{RPA})}_{eff}=\frac{1}{2}\sum_{S\in\mathcal{G}}\sum_{U\in\mathcal{G}}g_Sg_U\int_1\psi^\dagger(1)S\psi(1)\mathrm{Tr}\left[-SU+\frac{1}{2}S\gamma_1U\gamma_1+\frac{1}{2}S\gamma_2U\gamma_2\right]\psi^\dagger(1)U\psi(1)\frac{m}{4\pi}\ln s. \tag{A3}$$

Performing the traces gives

$$\Delta S^{(\mathrm{RPA})}_{eff}=-\int_1(2g^2_{A_2}[(\psi^\dagger A_2\psi)^2+(\psi^\dagger D_1\psi)^2]+4g^2_{D_2}(\psi^\dagger D_2\psi)^2+4g^2_\gamma[(\psi^\dagger C_3\psi)^2+(\psi^\dagger D_3\psi)^2])\frac{m}{4\pi}\ln s. \tag{A4}$$

For the second and third (vertex) diagrams in Fig. 2 we have the following terms:

$$\Delta S^{(V)}_{eff}=-\sum_{S\in\mathcal{G}}\sum_{U\in\mathcal{G}}g_Sg_U\int_1\int_2\psi^\dagger(1)SG(1-2)\times UG(2-1)S\psi(1)\psi^\dagger(2)U\psi(2). \tag{A5}$$

Performing the gradient expansion gives

$$\Delta S^{(V)}_{eff}=-\sum_{S\in\mathcal{G}}\sum_{U\in\mathcal{G}}g_Sg_U\int_1\psi^\dagger(1)S\left(-U+\frac{1}{2}\gamma_1U\gamma_1+\frac{1}{2}\gamma_2U\gamma_2\right)S\psi(1)\psi^\dagger(1)U\psi(1)\frac{m}{4\pi}\ln s. \tag{A6}$$

Performing the requisite sums and matrix algebra gives

$$\Delta S^{(V)}_{eff}=-\int_1\{g_{A_2}(-g_{A_1}+g_{D_2}+2g_\gamma)[(\psi^\dagger A_2\psi)^2+(\psi^\dagger D_1\psi)^2]-2g_{D_2}(g_{A_1}-2g_{A_2}+g_{D_2}+2g_\gamma)(\psi^\dagger D_2\psi)^2\}\frac{m}{4\pi}\ln s-\int_1\{-2g_\gamma(g_{A_1}-2g_{A_2}+g_{D_2})[(\psi^\dagger C_3\psi)^2+(\psi^\dagger D_3\psi)^2]\}\frac{m}{4\pi}\ln s. \tag{A7}$$

For the fourth and fifth diagrams in Fig. 2 we find the following terms:

$$\Delta S_{eff}^{(L)} = -\frac{1}{4}\sum_{S,U\in\mathcal{G}} g_S g_U \int_1 \left\{ [\psi^\dagger(1)[S,U]\psi(1)]^2 + \frac{1}{2}\sum_{a=1}^{2} [\psi^\dagger(1) \times (S\gamma_a U + U\gamma_a S)\psi(1)]^2 \right\} \frac{m}{4\pi} \ln s. \quad \text{(A8)}$$

The corresponding change in the effective action is

$$\begin{aligned}\Delta S_{eff}^{(L)} = &-\int_1 \left\{ 2g_{A_1}g_{A_2}(\psi^\dagger A_1\psi)^2 + \frac{1}{2}(g_{A_1}^2 + 4g_{A_2}^2 - 4g_{A_2}g_{D_2} \right. \\ &\left. + 2g_{D_2}^2 + 2g_\gamma^2)[(\psi^\dagger A_2\psi)^2 + (\psi^\dagger D_1\psi)^2] \right\} \\ &-\int_1 \{2g_{A_2}(g_{D_2} - g_{A_2})(\psi^\dagger D_2\psi)^2 + 2g_{A_2}g_\gamma[(\psi^\dagger C_3\psi)^2 \\ &+ (\psi^\dagger D_3\psi)^2] - 2g_\gamma^2(\psi^\dagger B_2\psi)^2\} - \int_1 \{(g_{D_2} \\ &- 2g_{A_2})g_\gamma[(\psi^\dagger A_4\psi)^2 + (\psi^\dagger B_4\psi)^2 + (\psi^\dagger C_4\psi)^2 \\ &+ (\psi^\dagger D_4\psi)^2]\}. \end{aligned} \quad \text{(A9)}$$

In order to find the renormalization of the coupling constants, the last two terms must be rewritten using the Fierz identities [Eqs. (52) and (56)]. Adding the terms from $\Delta\mathcal{S}_{eff}^{(\mathrm{RPA})}$, $\Delta\mathcal{S}_{eff}^{(V)}$, and $\Delta\mathcal{S}_{eff}^{(L)}$, rescaling the fields and the integration measure, and comparing to the starting action [Eq. (57)] we find the RG equations [Eq. (60)] for the four coupling constants in the spinless case.

The above Eqs. (A2), (A5), and (A8) can also be used to derive the flow equations of the nine coupling constants in the case of spin-1/2 fermions. In this case, we have $\mathcal{G}=\{A_1\otimes 1, A_2\otimes 1, D_1\otimes 1, B_1\otimes 1, C_2\otimes 1, B_2\otimes 1, C_1\otimes 1, D_2\otimes 1, A_3\otimes 1, B_3\otimes 1, B_4\otimes 1, A_4\otimes 1, C_4\otimes 1, D_4\otimes 1, C_3\otimes 1, D_3\otimes 1\}$ and the corresponding couplings, in order of appearance of S in $\mathcal{G}$, are

$$\{g_{A_1}^{(c)}, g_{A_2}^{(c)}, g_{A_2}^{(c)}, g_{B_1}^{(c)}, g_{B_1}^{(c)}, g_{B_2}^{(c)}, g_{C_1}^{(c)}, g_{D_2}^{(c)}, g_\alpha^{(c)}, g_\alpha^{(c)}, g_\beta^{(c)}, g_\beta^{(c)}, g_\beta^{(c)}, g_\beta^{(c)}, g_\gamma^{(c)}, g_\gamma^{(c)}\}.$$

The resulting RG flow equations for spin-1/2 fermions are

$$\frac{dg_{A_1}^{(c)}}{d\ln s} = -4(g_{A_1}^{(c)}g_{A_2}^{(c)} + g_{B_1}^{(c)}g_{B_2}^{(c)} + 2g_\alpha^{(c)}g_\beta^{(c)})\frac{m}{4\pi}, \quad \text{(A10)}$$

$$\begin{aligned}\frac{dg_{A_2}^{(c)}}{d\ln s} = \{&-g_{A_1}^{(c)2} + 2g_{A_1}^{(c)}g_{A_2}^{(c)} - 12g_{A_2}^{(c)2} - g_{B_2}^{(c)2} - (g_{C_1}^{(c)} - 2g_{B_1}^{(c)})^2 \\ &- g_{D_2}^{(c)2} + 2g_{A_2}^{(c)}(g_{B_2}^{(c)} - g_{C_1}^{(c)} + g_{D_2}^{(c)} + 2g_\alpha^{(c)} - 2g_\gamma^{(c)}) \\ &- 2[g_\alpha^{(c)2} + (g_\gamma^{(c)} - 2g_\beta^{(c)})^2]\}\frac{m}{4\pi}, \end{aligned} \quad \text{(A11)}$$

$$\begin{aligned}\frac{dg_{B_1}^{(c)}}{d\ln s} = \{&2g_{B_1}^{(c)}(g_{A_1}^{(c)} - 4g_{B_1}^{(c)} - 4g_{A_2}^{(c)} + g_{B_2}^{(c)} - g_{C_1}^{(c)} + g_{D_2}^{(c)} - 2g_\alpha^{(c)} \\ &+ 2g_\gamma^{(c)}) - 2[g_{A_1}^{(c)}g_{B_2}^{(c)} - g_{C_1}^{(c)}(2g_{A_2}^{(c)} - g_{D_2}^{(c)}) - 2g_\alpha^{(c)}(2g_\beta^{(c)} \\ &- g_\gamma^{(c)})]\}\frac{m}{4\pi}, \end{aligned}$$

$$\begin{aligned}\frac{dg_{B_2}^{(c)}}{d\ln s} = &-4(g_{A_1}^{(c)}g_{B_1}^{(c)} + g_{A_2}^{(c)}g_{B_2}^{(c)} - g_\alpha^{(c)2} - 2g_\beta^{(c)2} + 2g_\beta^{(c)}g_\gamma^{(c)} \\ &- g_\gamma^{(c)2})\frac{m}{4\pi}, \end{aligned} \quad \text{(A12)}$$

$$\begin{aligned}\frac{dg_{C_1}^{(c)}}{d\ln s} = &4[g_{C_1}^{(c)}(g_{A_1}^{(c)} - 3g_{A_2}^{(c)} - 2g_{B_1}^{(c)} + g_{B_2}^{(c)} - 3g_{C_1}^{(c)} + g_{D_2}^{(c)} - 2g_\alpha^{(c)} \\ &+ 4g_\beta^{(c)} - 2g_\gamma^{(c)}) + g_{B_1}^{(c)}(2g_{A_2}^{(c)} - g_{D_2}^{(c)}) - 2g_\alpha^{(c)}(g_\beta^{(c)} \\ &- g_\gamma^{(c)})]\frac{m}{4\pi} \end{aligned} \quad \text{(A13)}$$

$$\begin{aligned}\frac{dg_{D_2}^{(c)}}{d\ln s} = &4[g_{D_2}^{(c)}(g_{A_1}^{(c)} - 3g_{A_2}^{(c)} - 2g_{B_1}^{(c)} + g_{B_2}^{(c)} + g_{C_1}^{(c)} - 3g_{D_2}^{(c)} + 2g_\alpha^{(c)} \\ &- 4g_\beta^{(c)} + 2g_\gamma^{(c)}) + g_{A_2}^{(c)2} + g_{B_1}^{(c)}(g_{B_1}^{(c)} - g_{C_1}^{(c)}) + 2g_\beta^{(c)}(g_\beta^{(c)} \\ &- g_\gamma^{(c)})]\frac{m}{4\pi}, \end{aligned} \quad \text{(A14)}$$

$$\begin{aligned}\frac{dg_\alpha^{(c)}}{d\ln s} = &-4[g_\alpha^{(c)}(g_{A_2}^{(c)} - g_{B_2}^{(c)}) + g_\beta^{(c)}(g_{A_1}^{(c)} - 2g_{B_1}^{(c)} + g_{C_1}^{(c)}) + g_\gamma^{(c)}(g_{B_1}^{(c)} \\ &- g_{C_1}^{(c)})]\frac{m}{4\pi}, \end{aligned} \quad \text{(A15)}$$

$$\begin{aligned}\frac{dg_\beta^{(c)}}{d\ln s} = &2[g_\beta^{(c)}(g_{A_1}^{(c)} - 4g_{A_2}^{(c)} + g_{B_2}^{(c)} + g_{C_1}^{(c)} + g_{D_2}^{(c)} - 4g_\beta^{(c)}) - g_\alpha^{(c)}(g_{A_1}^{(c)} \\ &- 2g_{B_1}^{(c)} + g_{C_1}^{(c)}) + g_\gamma^{(c)}(2g_{A_2}^{(c)} - g_{B_2}^{(c)} - g_{D_2}^{(c)})]\frac{m}{4\pi}, \end{aligned} \quad \text{(A16)}$$

$$\begin{aligned}\frac{dg_\gamma^{(c)}}{d\ln s} = &-4[g_\alpha^{(c)}(g_{B_1}^{(c)} - g_{C_1}^{(c)}) + g_\beta^{(c)}(g_{B_2}^{(c)} - 2g_{A_2}^{(c)} + g_{D_2}^{(c)}) - g_\gamma^{(c)}(g_{A_1}^{(c)} \\ &- 3g_{A_2}^{(c)} + 2g_{B_1}^{(c)} - g_{C_1}^{(c)} + g_{D_2}^{(c)} - 4g_\gamma^{(c)})]\frac{m}{4\pi}. \end{aligned} \quad \text{(A17)}$$

APPENDIX B: FIERZ REDUCTION FOR SPIN-$\frac{1}{2}$ case

If we arrange the quartic contact terms into an 18-dimensional vector

$$\begin{aligned}\mathcal{V} = \{&(\psi_\alpha^\dagger A_1 \psi_\alpha)^2, (\psi_\alpha^\dagger A_2 \psi_\alpha)^2 + (\psi_\alpha^\dagger D_1 \psi_\alpha)^2, (\psi_\alpha^\dagger B_1 \psi_\alpha)^2 + (\psi_\alpha^\dagger C_2 \psi_\alpha)^2, (\psi_\alpha^\dagger B_2 \psi_\alpha)^2, (\psi_\alpha^\dagger C_1 \psi_\alpha)^2, (\psi_\alpha^\dagger D_2 \psi_\alpha)^2, (\psi_\alpha^\dagger A_3 \psi_\alpha)^2 \\ &+ (\psi_\alpha^\dagger B_3 \psi_\alpha)^2, \sum_{X=A,B,C,D} (\psi_\alpha^\dagger X_4 \psi_\alpha)^2, (\psi_\alpha^\dagger C_3 \psi_\alpha)^2 + (\psi_\alpha^\dagger D_3 \psi_\alpha)^2, (\psi_\alpha^\dagger A_1 \vec{\sigma}_{\alpha\beta} \psi_\beta)^2, (\psi_\alpha^\dagger A_2 \vec{\sigma}_{\alpha\beta} \psi_\beta)^2 + (\psi_\alpha^\dagger D_1 \vec{\sigma}_{\alpha\beta} \psi_\beta)^2, (\psi_\alpha^\dagger B_1 \vec{\sigma}_{\alpha\beta} \psi_\beta)^2 \\ &+ (\psi_\alpha^\dagger C_2 \vec{\sigma}_{\alpha\beta} \psi_\beta)^2, (\psi_\alpha^\dagger B_2 \vec{\sigma}_{\alpha\beta} \psi_\beta)^2, (\psi_\alpha^\dagger C_1 \vec{\sigma}_{\alpha\beta} \psi_\beta)^2, (\psi_\alpha^\dagger D_2 \vec{\sigma}_{\alpha\beta} \psi_\beta)^2, (\psi_\alpha^\dagger A_3 \vec{\sigma}_{\alpha\beta} \psi_\beta)^2 \\ &+ (\psi_\alpha^\dagger B_3 \vec{\sigma}_{\alpha\beta} \psi_\beta)^2, \sum_{X=A,B,C,D} (\psi_\alpha^\dagger X_4 \vec{\sigma}_{\alpha\beta} \psi_\beta)^2, (\psi_\alpha^\dagger C_3 \vec{\sigma}_{\alpha\beta} \psi_\beta)^2 + (\psi_\alpha^\dagger D_3 \vec{\sigma}_{\alpha\beta} \psi_\beta)^2\}, \end{aligned} \tag{B1}$$

then the Fierz identities [Eq. (106)] can be used to relate different components of $\mathcal{V}$ via the linear constraint $\mathcal{F}\mathcal{V}=0$.

In practice, to obtain the Fierz matrix $\mathcal{F}$ we arrange the 64 $SU(8)$ generators Λ^a in the order $\{X\otimes 1, X\otimes\sigma^z, X\otimes\sigma^x, X\otimes\sigma^y\}$, where $X=\{A_1,A_2,D_1,B_1,C_2,B_2,C_1,D_2,A_3,B_3,B_4,A_4,C_4,D_4,C_3,D_3\}$. Straightforwardly, a 64-component analog of the Fierz vector, obtained by using our ordered set of $SU(8)$ generators, will be denoted by $\tilde{\mathcal{V}}$. Next, we notice that only the (diagonal) terms with $S=T$ enter our $\mathcal{L}_{int}$, and that $\mathrm{Tr}[S\Lambda^a S\Lambda^b]\sim\delta_{ab}$. Therefore, for Λ^a arranged as described above, we numerically generate a 64×64 matrix $\tilde{\Phi}_{ab}=-\mathrm{Tr}[\Lambda^a\Lambda^b\Lambda^a\Lambda^b]/64$. We then construct an auxiliary 64×64 matrix

$$\mathcal{M} = \begin{pmatrix} \mathcal{Q} & 0 & 0 & 0 \\ 0 & \mathcal{Q} & \mathcal{Q} & \mathcal{Q} \\ 0 & 2\mathcal{Q} & -\mathcal{Q} & -\mathcal{Q} \\ 0 & 0 & \mathcal{Q} & -\mathcal{Q} \end{pmatrix},$$

where

$$\mathcal{Q} = \begin{pmatrix} 1 & 0 & 0 & 0 & 0 & 0 & 0 & 0 & 0 & 0 & 0 & 0 & 0 & 0 & 0 & 0 \\ 0 & 1 & 1 & 0 & 0 & 0 & 0 & 0 & 0 & 0 & 0 & 0 & 0 & 0 & 0 & 0 \\ 0 & 0 & 0 & 1 & 1 & 0 & 0 & 0 & 0 & 0 & 0 & 0 & 0 & 0 & 0 & 0 \\ 0 & 0 & 0 & 0 & 0 & 1 & 0 & 0 & 0 & 0 & 0 & 0 & 0 & 0 & 0 & 0 \\ 0 & 0 & 0 & 0 & 0 & 0 & 1 & 0 & 0 & 0 & 0 & 0 & 0 & 0 & 0 & 0 \\ 0 & 0 & 0 & 0 & 0 & 0 & 0 & 1 & 0 & 0 & 0 & 0 & 0 & 0 & 0 & 0 \\ 0 & 0 & 0 & 0 & 0 & 0 & 0 & 0 & 1 & 1 & 0 & 0 & 0 & 0 & 0 & 0 \\ 0 & 0 & 0 & 0 & 0 & 0 & 0 & 0 & 0 & 0 & 1 & 1 & 1 & 1 & 0 & 0 \\ 0 & 0 & 0 & 0 & 0 & 0 & 0 & 0 & 0 & 0 & 0 & 0 & 0 & 0 & 1 & 1 \\ 0 & -1 & 1 & 0 & 0 & 0 & 0 & 0 & 0 & 0 & 0 & 0 & 0 & 0 & 0 & 0 \\ 0 & 0 & 0 & -1 & 1 & 0 & 0 & 0 & 0 & 0 & 0 & 0 & 0 & 0 & 0 & 0 \\ 0 & 0 & 0 & 0 & 0 & 0 & 0 & 0 & -1 & 1 & 0 & 0 & 0 & 0 & 0 & 0 \\ 0 & 0 & 0 & 0 & 0 & 0 & 0 & 0 & 0 & 0 & -1 & 1 & -1 & 1 & 0 & 0 \\ 0 & 0 & 0 & 0 & 0 & 0 & 0 & 0 & 0 & 0 & -1 & -1 & 1 & 1 & 0 & 0 \\ 0 & 0 & 0 & 0 & 0 & 0 & 0 & 0 & 0 & 0 & 1 & -1 & -1 & 1 & 0 & 0 \\ 0 & 0 & 0 & 0 & 0 & 0 & 0 & 0 & 0 & 0 & 0 & 0 & 0 & 0 & -1 & 1 \end{pmatrix}$$

in order to write

$$\tilde{\mathcal{V}} = \tilde{\Phi}\tilde{\mathcal{V}} \Rightarrow \mathcal{M}\tilde{\mathcal{V}} = (\mathcal{M}\tilde{\Phi}\mathcal{M}^{-1})\mathcal{M}\tilde{\mathcal{V}}.$$

It is easily seen that components 1–9 and 17–25 of $\mathcal{M}\tilde{\mathcal{V}}$ correspond to our Fierz vector $\mathcal{V}$. Moreover, the blocks 1–9 and 17–25 of the matrix $\mathcal{M}\tilde{\Phi}\mathcal{M}^{-1}$ do not couple to the rest of the components, and, when subtracted from an 18-dimensional unit matrix, correspond to the sought Fierz matrix,

$$\mathcal{F}=\begin{pmatrix}
9 & 1 & 1 & 1 & 1 & 1 & 1 & 1 & 1 & 1 & 1 & 1 & 1 & 1 & 1 & 1 & 1 & 1 \\
2 & 8 & 0 & 2 & -2 & -2 & 2 & 0 & -2 & 2 & 0 & 0 & 2 & -2 & -2 & 2 & 0 & -2 \\
2 & 0 & 8 & 2 & -2 & -2 & -2 & 0 & 2 & 2 & 0 & 0 & 2 & -2 & -2 & -2 & 0 & 2 \\
1 & 1 & 1 & 9 & 1 & 1 & -1 & -1 & -1 & 1 & 1 & 1 & 1 & 1 & 1 & -1 & -1 & -1 \\
1 & -1 & -1 & 1 & 9 & 1 & -1 & 1 & -1 & 1 & -1 & -1 & 1 & 1 & 1 & -1 & 1 & -1 \\
1 & -1 & -1 & 1 & 1 & 9 & 1 & -1 & 1 & 1 & -1 & -1 & 1 & 1 & 1 & 1 & -1 & 1 \\
2 & 2 & -2 & -2 & -2 & 2 & 8 & 0 & 0 & 2 & 2 & -2 & -2 & -2 & 2 & 0 & 0 & 0 \\
4 & 0 & 0 & -4 & 4 & -4 & 0 & 8 & 0 & 4 & 0 & 0 & -4 & 4 & -4 & 0 & 0 & 0 \\
2 & -2 & 2 & -2 & -2 & 2 & 0 & 0 & 8 & 2 & -2 & 2 & -2 & -2 & 2 & 0 & 0 & 0 \\
3 & 3 & 3 & 3 & 3 & 3 & 3 & 3 & 3 & 7 & -1 & -1 & -1 & -1 & -1 & -1 & -1 & -1 \\
6 & 0 & 0 & 6 & -6 & -6 & 6 & 0 & -6 & -2 & 8 & 0 & -2 & 2 & 2 & -2 & 0 & 2 \\
6 & 0 & 0 & 6 & -6 & -6 & -6 & 0 & 6 & -2 & 0 & 8 & -2 & 2 & 2 & 2 & 0 & -2 \\
3 & 3 & 3 & 3 & 3 & 3 & -3 & -3 & -3 & -1 & -1 & -1 & 7 & -1 & -1 & 1 & 1 & 1 \\
3 & -3 & -3 & 3 & 3 & 3 & -3 & 3 & -3 & -1 & 1 & 1 & -1 & 7 & -1 & 1 & -1 & 1 \\
3 & -3 & -3 & 3 & 3 & 3 & 3 & -3 & 3 & -1 & 1 & 1 & -1 & -1 & 7 & -1 & 1 & -1 \\
6 & 6 & -6 & -6 & -6 & 6 & 0 & 0 & 0 & -2 & -2 & 2 & 2 & 2 & -2 & 8 & 0 & 0 \\
12 & 0 & 0 & -12 & 12 & -12 & 0 & 0 & 0 & -4 & 0 & 0 & 4 & -4 & 4 & 0 & 8 & 0 \\
6 & -6 & 6 & -6 & -6 & 6 & 0 & 0 & 0 & -2 & 2 & -2 & 2 & 2 & -2 & 0 & 0 & 8
\end{pmatrix}. \tag{B2}$$

One can check that the above matrix has nine zero eigenvalues, which implies nine independent couplings and nine constraints. In addition, one can solve the linear system $\mathcal{F}\mathcal{V}=0$ and eliminate all terms of the form $(\psi_\alpha^\dagger X_j \vec{\sigma}_{\alpha\beta}\psi_\beta)^2$ in favor of $(\psi_\alpha^\dagger X_j \psi_\alpha)^2$.

[1] E. McCann and V. I. Fal'ko, Phys. Rev. Lett. **96**, 086805 (2006).
[2] A. H. Castro Neto, F. Guinea, N. M. R. Peres, K. S. Novoselov, and A. K. Geim, Rev. Mod. Phys. **81**, 109 (2009).
[3] O. Vafek and K. Yang, Phys. Rev. B **81**, 041401 (2010).
[4] F. Zhang, H. Min, M. Polini, and A. H. MacDonald, Phys. Rev. B **81**, 041402 (2010).
[5] R. Nandkishore and L. Levitov, Phys. Rev. Lett. **104**, 156803 (2010).
[6] Y. Lemonik, I. Aleiner, C. Toke, and V. Fal'ko, arXiv:1006.1399 (unpublished).
[7] H. Min, G. Borghi, M. Polini, and A. H. MacDonald, Phys. Rev. B **77**, 041407 (2008).
[8] K. Sun, H. Yao, E. Fradkin, and S. A. Kivelson, Phys. Rev. Lett. **103**, 046811 (2009).
[9] S. Raghu, S. A. Kivelson, and D. J. Scalapino, Phys. Rev. B **81**, 224505 (2010).
[10] K. S. Novoselov, E. McCann, S. V. Morozov, V. I. Fal'Ko, M. I. Katsnelson, U. Zeitler, D. Jiang, F. Schedin, and A. K. Geim, Nat. Phys. **2**, 177 (2006).
[11] B. E. Feldman, J. Martin, and A. Yacoby, Nat. Phys. **5**, 889 (2009).
[12] Y. Zhao, P. Cadden-Zimansky, Z. Jiang, and P. Kim, Phys. Rev. Lett. **104**, 066801 (2010).
[13] T. Ohta, A. Bostwick, T. Seyller, K. Horn, and E. Rotenberg, Science **313**, 951 (2006).
[14] J. Yan, E. A. Henriksen, P. Kim, and A. Pinczuk, Phys. Rev. Lett. **101**, 136804 (2008).
[15] Y. Zhang, T. Tang, C. Girit, Z. Hao, M. C. Martin, A. Zettl, M. F. Crommie, Y. R. Shen, and F. Wang, Nature **459**, 820 (2009).
[16] R. Nandkishore and L. Levitov, arXiv:1002.1966 (unpublished).
[17] I. F. Herbut, V. Juričić, and B. Roy, Phys. Rev. B **79**, 085116 (2009).
[18] G. L. Bir and G. E. Pikus, *Symmetry and Strain-Indused Effects in Semiconductors* (Wiley, New York, 1974).
[19] I. L. Aleiner, D. E. Kharzeev, and A. M. Tsvelik, Phys. Rev. B **76**, 195415 (2007).
[20] L. M. Zhang, Z. Q. Li, D. N. Basov, M. M. Fogler, Z. Hao, and M. C. Martin, Phys. Rev. B **78**, 235408 (2008).
[21] J. Nilsson, A. H. Castro Neto, F. Guinea, and N. M. R. Peres, Phys. Rev. B **78**, 045405 (2008).
[22] R. Shankar, Rev. Mod. Phys. **66**, 129 (1994).
[23] C. Itzykson and J.-B. Zuber, *Quantum Field Theory* (Dover, Mineola, NY, 2005), p. 161.
[24] F. D. M. Haldane, Phys. Rev. Lett. **61**, 2015 (1988).
[25] E. Fradkin, *Field Theories of Condensed Matter Systems* (Addison-Wesley, Redwood City, CA, 1991), Chap. 2.
[26] T. Paiva, R. T. Scalettar, W. Zheng, R. R. P. Singh, and J. Oitmaa, Phys. Rev. B **72**, 085123 (2005).